# Targeting Putrescine Homeostasis with *Lactiplantibacillus plantarum* PS128 to Mitigate Autism-like Behaviors in *Fmr1* KO Mice

Yingmin Cui,[1, 5] Yingxuan Chen,[1, 5] Yen-Wenn Liu,[2, 5] Shan Zheng,[1] Jialong Cui,[3] Tianan Li,[1] Ying-Chieh Tsai,[2] Shanshan Gu,[4] Ji Ma,[1] Wei Zhang,[1] Haipeng Li,[4] Xiao-Bing Yuan,[1, *] Yi-Hsuan Pan[1, 6, *]

[1]Key Laboratory of Brain Functional Genomics of Shanghai and Ministry of Education, Institute of Brain Functional Genomics, School of Life Science and the Collaborative Innovation Center for Brain Science, East China Normal University, Shanghai 200062, China
[2]Institute of Biochemistry and Molecular Biology, National Yang-Ming University, Taipei 11221, Taiwan
[3]Institute of Mechanobiology and Medical Engineering, School of Life Sciences and Biotechnology, Shanghai Jiao Tong University, Shanghai 201100, China
[4]Shanghai Institute of Nutrition and Health, University of Chinese Academy of Sciences, Chinese Academy of Sciences, Shanghai 200031, China.
[5]These authors contributed equally
[6]Lead contact
*Correspondence: yxpan@sat.ecnu.edu.cn (Y.H.P.), xbyuan@brain.ecnu.edu.cn (X.B.Y.)

## SUMMARY

Autism spectrum disorder (ASD) often presents with gastrointestinal disturbances, yet the molecular mechanisms linking gut alterations to behavioral dysfunction remain incompletely understood. Using Fragile X mental retardation 1 (*Fmr1*) knockout mice, we found that autism-like behaviors are associated with disrupted gut microbiota–polyamine metabolism and elevated putrescine in the prefrontal cortex (PFC). Supplementation with *Lactiplantibacillus plantarum* PS128 reshaped gut microbial communities, improved intestinal integrity, and restored arginine–ornithine–polyamine metabolic homeostasis. PS128 normalized the serum-to-PFC putrescine imbalance and reduced expression of putrescine transporters in the PFC. Consistent with a causal role, peripheral putrescine elevation induced autism-like behaviors in wild-type mice, whereas inhibition of putrescine synthesis ameliorated behavioral deficits in *Fmr1* knockout mice. Together, these findings identify putrescine dysregulation as an important metabolic contributor to autism-like phenotypes, support a metabolically stratifiable ASD subtype, and implicate PS128 as a psychobiotic intervention acting through the microbiota–gut–brain axis.

## KEYWORDS

Gut microbiota–metabolite–brain axis; polyamine; Fragile X mental retardation 1; prefrontal cortex

## INTRODUCTION

Autism spectrum disorder (ASD) encompasses a group of neurodevelopmental conditions characterized by deficits in social interaction and communication, accompanied by repetitive and restricted behaviors and interests. Both genetic and environmental factors contribute to ASD, with genetic influences playing a central role.[1] In recent years, ASD has emerged as a major public health concern due to its rising global prevalence.[2,3] However, effective therapies targeting the core symptoms of ASD remain limited.[4] Growing evidence implicates metabolic disturbances in ASD pathophysiology, particularly involving amino acid metabolism, including branched-chain amino acids (BCAAs), arginine, and ornithine.[5-8]

Microbial metabolites are increasingly recognized as key modulators of host physiology, with several shown to influence brain function through the gut–brain axis.[9,10] Among the diverse classes of host- and microbiota-derived metabolites, putrescine is a polyamine primarily derived from arginine and ornithine catabolism. Putrescine interacts electrostatically with nucleic acids, proteins, lipids, and proteoglycans, thereby regulating gene expression, oxidative stress, cell proliferation, and inflammation.[11] Polyamine homeostasis is tightly regulated, and the intestinal microbiota represents a major exogenous source.[12] Notably, elevated levels of putrescine and its derivative spermine have been detected in the saliva of children with ASD,[13] implicating polyamine imbalance in ASD pathophysiology.

Probiotics, particularly psychobiotics, have attracted increasing interest as safe and accessible interventions capable of reshaping the gut microbiome and modulating neurobehavioral outcomes.[14] Clinical evidence indicates that daily supplementation with *Lactiplantibacillus plantarum* PS128 (PS128) has been associated with improvements in social behaviors and attention-related symptoms in individuals with ASD, with minimal adverse effects.[15,16] However, the molecular pathways through which PS128 acts along the gut–brain axis to ameliorate ASD symptoms remain poorly defined. Fragile X mental retardation protein (FMRP), an RNA-binding protein encoded by the *Fmr1* gene, represents the most common monogenic cause of ASD,[17] and its deficiency leads to both gastrointestinal and behavioral abnormalities in humans and mice.[18,19] Accordingly, the *Fmr1* knockout (KO) mouse[20] provides a well-established model for dissecting gut–brain interactions in ASD and for uncovering the molecular mechanisms by which PS128 may exert therapeutic effects.

In this study, we investigated whether supplementation with *Lactiplantibacillus plantarum* PS128 alleviates autism-like phenotypes in *Fmr1* knockout mice. We identified disruption of the arginine–ornithine–polyamine metabolic pathway in the gut of KO mice and found that PS128 supplementation reshaped the gut microbiota and restored peripheral–central putrescine balance. This effect was accompanied by enrichment of beneficial bacterial taxa and suppression of inflammation- and disease-associated taxa in the gut, together with reduced expression of putrescine transporters in the prefrontal cortex (PFC). Furthermore, bidirectional manipulation of putrescine levels demonstrated a causal contribution of putrescine to autism-like phenotypes. Together, these findings suggest putrescine as a candidate metabolic biomarker and therapeutic target for ASD.

## RESULTS

### PS128 treatment substantially ameliorates autism-like behaviors in *Fmr1* KO mice

To determine whether PS128 treatment mitigates behavioral abnormalities in *Fmr1* knockout (KO) mice, we provided PS128-containing jelly every other day by voluntary oral consumption to KO mice and their wild-type (WT) littermates (Video S1). Behavioral performance was assessed using a comprehensive battery, including the open-field test (OFT), elevated plus maze (EPM), O-maze test (OMT), novel object recognition test (NORT), reciprocal social interaction test (RSIT), balance beam test (BBT), olfactory habituation/dishabituation test (OHDT), and tube test (TT) throughout the treatment period. These assays were selected to capture ASD-relevant behavioral domains, including anxiety-related behavior, repetitive and stereotypic behaviors, social interaction and novelty preference, and motor coordination.

Across most behavioral assays, PS128 treatment had minimal effects on WT mice (Figures 1 and S1), and the behavioral alterations were primarily observed in *Fmr1* KO mice. In the OFT (Figures 1A and S1A), KO mice exhibited significantly reduced total and central exploration distances compared with WT controls (Figures 1B and 1C), indicating enhanced anxiety-like behavior. PS128 treatment restored these measures toward WT levels (Figures 1A–1C) and increased the time KO mice spent in the center zone (Figures S1B and S1C). These findings indicate that PS128 alleviates anxiety-like behavior in KO mice. No significant differences were detected in the EPM or OMT (Figures S1D–S1I), suggesting that anxiety-related abnormalities in KO mice are context dependent.

In the NORT (Figure 1D), KO mice showed a reduced recognition index (Figure 1E) and excessive climbing on both familiar and novel objects (Figure 1F), reflecting repetitive and stereotypic behaviors.[21] Similar repetitive climbing behavior was also observed in the OHDT (Figures S1J–S1N, Videos S2 and S3), where KO mice frequently climbed and remained on the swab (Figure S1J). PS128 supplementation ameliorated both recognition deficits and stereotypic behaviors, restoring the recognition index to WT levels and markedly reducing abnormal climbing.

In the RSIT (Figure 1G), WT and WTPS mice displayed comparable interaction patterns (Figure S1O). WT mice preferentially interacted with a novel mouse (Stage 3) over a familiar one (Stage 2), whereas KO mice did not (Figures 1H and 1I), indicating impaired social novelty preference. PS128 treatment significantly improved social novelty preference and recognition performance in KO mice (Figures 1D–1I).

In the BBT (Figure 1J), KO mice required more time to traverse both 30° and 60° beams (Figures 1K and 1L), indicating impaired motor coordination. PS128 intervention reduced traversal times in KO mice, although performance did not fully reach WT levels. In the TT (Figure S1P), PS128-treated KO mice (KOPS) displayed a higher probability of forward movement against unfamiliar KO or WT opponents (Figures S1Q and S1R), implicating enhanced social confidence. Collectively, PS128 treatment mitigated core autism-like phenotypes in *Fmr1* KO mice (Figures 1 and S1).

## PS128 reshapes the gut microbiota and suppresses inflammation- and disease-associated taxa in *Fmr1* KO mice

To elucidate the microbiota changes underlying the behavioral improvements of *Fmr1* KO mice in response to PS128 intervention, we performed 16S rRNA sequencing and metagenomic profiling on fecal samples, together with fluorescence imaging of gut tissues, collected from KO mice and WT littermates before and during PS128 supplementation.

At baseline, prior to PS128 supplementation, 1-month-old KO mice (KO-1M) exhibited significantly lower α-diversity than age-matched WT littermates (WT-1M) (Figures 2A and 2B) and a distinct β-diversity profile (Figure 2C). WT-1M mice harbored several beneficial genera, including *Bifidobacterium*, *Anaerostipes*, and *Blautia* (Figure 2D), which are known to promote mucus secretion, protect against enteric pathogens, and modulate mucosal immunity.[22] In contrast, KO-1M mice showed increased abundances of the pathogenic genera *Helicobacter* and *Chlamydia* (Figure 2D), both of which have been linked to gastrointestinal inflammation and neurobehavioral abnormalities.[23,24]

By four months of age, KO mice (KO-4M) maintained reduced α-diversity (Figures S2A and S2B) and distinct β-diversity (Figure 2E) relative to WT-4M mice, along with persistently elevated *Helicobacter* and *Chlamydia* (Figure 2F). Spearman correlation analysis further revealed positive correlations between the abundances of these taxa and behavioral deficits in KO-4M mice (Figure 2G), including reduced social interaction time (RSIT), prolonged traversal latency (BBT), and impaired tube test (TT) performance.

Upon PS128 intervention, fluorescence imaging demonstrated preferential retention and colonization of PS128 in the cecum and colon of both WT and KO mice (Figures 2H–2J and S3), and in the stomach and small intestine of WT mice (Figures S3A, S3F, and S3N). Colonization coincided with pronounced microbiota remodeling (Figures 2K, 2L, and S2C–S2E). Notably, PS128-treated KO mice (KOPS-4M) exhibited α-diversity comparable to WT-4M littermates (Figures S2F and S2G) and a distinct β-diversity profile relative to untreated KO-4M mice (Figure 2M). KOPS-4M mice also showed marked enrichment of *Lactiplantibacillus* and *Bifidobacterium*, together with significant reductions in *Ileibacterium*, *Enterorhabdus*, *Helicobacter*, and *Chlamydia* (Figures 2K, 2L, 2N–2P and S2H–S2M). Overall, these findings indicate that PS128 treatment reshapes the gut microbiota by suppressing inflammation- and disease-associated taxa while enriching beneficial *Lactiplantibacillus* and *Bifidobacterium*. These microbiota shifts coincide with the observed improvements in behavioral phenotypes.

## PS128 ameliorates gut barrier dysfunction and enhances intestinal integrity in *Fmr1* KO Mice

To determine whether PS128-induced microbiota remodeling was accompanied by improvements in intestinal structure and function, we performed anatomical, histological, and biological analyses, with WT littermates used as physiological references.

KO mice displayed significantly elevated intestinal permeability in the intestinal permeability assay (IPA), which was reduced following PS128 supplementation (Figures 3A and 3B). In addition, KO mice exhibited pronounced gastrointestinal abnormalities, including elongation of the cecum and colon (Figures 3C–3E), distorted crypt architecture (Figures 3F and 3G), and reduced goblet cell numbers (Figures 3H–3J), as well as diminished MUC2-positive areas (Figures 3K–3M). PS128 treatment alleviated these abnormalities, restoring mucosal architecture and enhancing epithelial barrier integrity. Collectively, these results demonstrate that PS128 supplementation improves intestinal barrier structure and function in *Fmr1* KO mice.

## PS128 rebalances the Arg–Orn–polyamine metabolic pathway and scavenges putrescine in the gut of *Fmr1* KO

To investigate the functional consequences of PS128-induced microbiota remodeling, we reanalyzed the metagenomic datasets and performed whole-genome sequencing of the PS128 strain to assess its microbial metabolic potential in *Fmr1* KO mice.

Based on KEGG annotation, microbial functions in KO mice were primarily enriched in carbohydrate and amino acid metabolism (Figure S4A). Among these categories, amino acid metabolism showed the most pronounced difference between KO and WT mice, with the highest LDA score ($\log_{10} = 3.55$) (Figure S4B). PS128 treatment further enhanced amino acid–related pathway in KO mice (Figure S4C). These results highlight amino acid metabolic dysregulation as a prominent microbial feature associated with *Fmr1* deficiency and linked to physiological abnormalities.

We next reconstructed metagenome-assembled genomes (MAGs) by binning contigs derived from the metagenomic datasets[25] and identified gut–brain modules (GBMs) encoded by species-level genome bins (SGBs) (Figure 4A). GBMs were categorized into eight functional clusters according to their relevance to gut–brain metabolic pathways. Among these, “Neurotransmitter metabolism I” (glutamate metabolism), “Amino acid metabolism II” (serine metabolism), and “Amino acid metabolism I” (arginine metabolism) contained the largest numbers of modules. Notably, “Amino acid metabolism I” showed the clearest difference between WT and KO mice and exhibited the most substantial recovery following PS128 treatment (Figure 4B).

Proteins encoded by bins within “Amino acid metabolism I” were annotated and quantified (Figure 4C), and highly expressed proteins were visualized using radar plots (Figure 4D). Compared with WT littermates, KO mice displayed reduced abundance of spermidine/putrescine transport ATP-binding and substrate-binding proteins, along with the elevated levels of N-carbamoyl-putrescine amidase, indicating diminished bacterial uptake and increased microbial production of putrescine. KO mice also showed increased arginine decarboxylase and decreased ornithine carbamoyltransferase, reflecting upstream disruption of arginine and ornithine metabolism. PS128 supplementation normalized these protein expression patterns, resulting in a more balanced amino acid and polyamine metabolic profile in KOPS mice (Figure 4D).

Whole-genome sequencing of PS128 revealed genes involved in arginine biosynthesis and export, as well as in the uptake and degradation of spermidine and putrescine, whereas genes required for de novo polyamine biosynthesis were absent (Figure 4E). This genomic profile supports a putrescine-consuming role for PS128 in KO mice. In addition, functional annotation showed that PS128-enriched taxa, including *Lactiplantibacillus plantarum*, *Lactiplantibacillus paraplantarum*, and *Levilactobacillus brevis*, together with the six most abundant bacterial species, harbor complementary genetic capacities for arginine, ornithine, and polyamine uptake, degradation, and synthesis (Figure 4F). Taken together, these analyses define a coordinated microbial network through which PS128 modulates arginine–ornithine–polyamine metabolism in the gut of *Fmr1* KO mice.

186 **PS128 realigns the peripheral–central putrescine equilibrium by realigning gut–brain polyamine flux**
187 PS128 improved prefrontal cortex (PFC)–dependent social behaviors and reduced striatum (STR)–
188 associated repetitive behaviors in *Fmr1* KO mice (Figures 1 and S1). Given that these behavioral effects
189 coincided with PS128-induced remodeling of gut arginine–ornithine–polyamine metabolism (Figures 4 and
190 S4), we next examined whether peripheral metabolic changes were reflected in polyamine homeostasis
191 within the PFC and STR. To this end, we performed targeted metabolomic profiling of 40 neuroactive
192 substances, seven short-chain fatty acids (SCFAs), and four additional fatty acids in both brain regions
193 (Tables S1 and S2).
194 Volcano plot analysis revealed a marked elevation of putrescine in the PFC of KO mice relative to WT
195 littermates (Figure 5A), which was significantly attenuated by PS128 supplementation (Figure S5A). This
196 effect was largely region specific, as putrescine levels in the STR showed only modest group differences
197 (Figures S5B and S5C). No significant differences were detected among groups for the 11 fatty acids
198 measured in either brain region (Figures S5D–S5G). Because putrescine circulates systemically (Figure
199 5B), we next quantified serum putrescine using targeted UHPLC–MS/MS and calculated the PFC-to-serum
200 ratio. KO mice exhibited a significantly elevated ratio compared with WT controls (Figure 5C), whereas
201 PS128 supplementation largely normalized this imbalance (Figure 5D), indicating a coordinated adjustment
202 of peripheral and central putrescine distribution in *Fmr1* KO mice.
203 To explore molecular changes accompanying this adjustment (Figure 5D), we performed single-nucleus
204 RNA sequencing (snRNA-seq) on PFC tissue from KO and WT mice with or without PS128 treatment.
205 PS128 did not appreciably alter overall cell-type composition (Figures 5E, 5F, and S6A). However,
206 transcriptomic analysis revealed a predominance of downregulated genes following PS128 treatment
207 (Figure S6B). Downregulated genes were enriched for pathways related to chromosome organization,
208 glycoprotein metabolism, and macroautophagy (Figure S6C), whereas upregulated genes were associated
209 with telomere organization and protein folding (Figure S6D). Notably, pathways involved in polyamine
210 transmembrane transport were selectively downregulated in PS128-treated KO mice (Figure 5H).
211 These pathways included *Atp13a2*, *Atp13a3*, and *Atp13a4* (Figures S6B and S6E), which encode
212 mammalian P5B-type ATPases implicated in cellular polyamine handling. Reduced expression of ATP13A2
213 and ATP13A3 in PS128-treated KO mice (KOPS) was confirmed by Western blotting (Figures 5I–5K). In
214 addition, *Atp13a4*, which is enriched in astrocytes forming part of the blood–brain barrier (Figure S6F), also
215 exhibited reduced expression (Figure S6G). These results indicate that PS128 downregulates polyamine-
216 related transport pathways in the PFC, in parallel with the restoration of peripheral–central putrescine
217 equilibrium in *Fmr1* KO mice.
218
219 **Bidirectional manipulation of putrescine metabolism alters autism-like behaviors in mice**
220 To determine whether disturbance of putrescine metabolism contributes to autism-like behaviors, we
221 administered intraperitoneally putrescine dihydrochloride (200 mg/kg) to 2-month-old wild-type (WT) mice
222 (Figure 6A). Although this treatment did not significantly change putrescine levels in the prefrontal cortex
223 (PFC) (Figure S7A), it was sufficient to induce multiple autism-like behavioral abnormalities. Treated WT
224 mice showed reduced total exploration distance, center exploration distance, and center exploration time
225 in the open-field test (OFT) (Figures 6B–6F), impaired social interaction in the reciprocal social interaction
226 test (RSIT) (Figure 6G), and prolonged traversal time on the 30° balance beam (Figure 6H). These results
227 indicate that elevated peripheral putrescine (Figure S7B) is sufficient to evoke autism-like behavioral
228 phenotypes in WT mice.
229 We next examined whether reducing putrescine synthesis could ameliorate autism-like behaviors in *Fmr1*
230 KO mice. To this end, we used α-difluoromethylornithine (DFMO), an irreversible inhibitor of ornithine
231 decarboxylase (Figure 6I). Intraperitoneal DFMO administration (500 mg/kg) significantly lowered PFC
232 putrescine levels in both 1- and 2-month-old KO mice (Figures 6J and 6K). DFMO had no significant effect
233 on locomotor activity in the OFT (Figures 6L and 6M); however, compared with 2-month-old KO mice,
234 DFMO slightly reduced center exploration distance and time in 1-month-old KO mice (Figures S7C–S7F),

suggesting age-dependent effects on anxiety-like behavior. Despite this, DFMO treatment increased social interaction time in the RSIT (Figures 6N and S7G) and shortened traversal time on the 30° beam during the first trial of the balance beam test (BBT) (Figures 6O and 6P). Early DFMO intervention also improved performance on the 60° beam in KO mice (Figure 6Q). Moreover, DFMO-treated KO mice exhibited tube test performance comparable to that of PS128-treated KO mice (KOPS) (Figures 6R and S1R), achieving higher winning scores than untreated KO mice (Figures 6S and 6T).

Altogether, these results show that elevating putrescine is sufficient to induce autism-like behaviors, whereas pharmacological reduction of putrescine alleviates these deficits, supporting a causal role for putrescine imbalance in the behavioral abnormalities of *Fmr1* KO mice.

## DISCUSSION

In this study, we show that altered microbial composition and dysregulated arginine–ornithine–polyamine metabolism are closely linked to autism-like behaviors in *Fmr1* KO mice. PS128 supplementation reshaped the gut microbiota, improved gut integrity, and rebalanced putrescine homeostasis across the gut-brain axis, in part through coordinated regulation of microbial metabolism and host transport systems. Our data identify putrescine as a modulator of behavioral abnormalities and suggest that PS128 acts through an integrated microbial–metabolic–neuronal pathway. These findings provide a conceptual framework for metabolic stratification and psychobiotic-based interventions in autism spectrum disorder.

Autism spectrum disorder (ASD) has substantial etiologic and phenotypic heterogeneity.[4] Genetic and environmental factors converge on the microbiota–gut–brain axis, where altered microbial metabolism influences amino acid turnover, neurotransmitter synthesis, epithelial integrity, and immune signaling.[26] Consistent with prior observations, *Fmr1* KO mice in our study exhibited repetitive and restricted behaviors, social impairments, and motor coordination deficits. These behavioral deficits were accompanied by intestinal dysbiosis, barrier dysfunction, and metabolic imbalance. These features align with reports of altered amino acid, lipid, and xenobiotic metabolism in ASD[27] and with evidence linking mucosal barrier disruption[20] and microbial metabolite shifts to behavioral phenotypes.[28,29]

Sustained supplementation with *Lactiplantibacillus plantarum* PS128 (PS128) markedly alleviated autism-like behaviors in *Fmr1* KO mice. PS128 reduced the elevated abundances of *Helicobacter* and *Chlamydia*, two taxa highly correlated with autism-like behaviors in untreated *Fmr1* KO mice, and restored beneficial genera, such as *Lactiplantibacillus* and *Bifidobacterium*. While modulation of microbial composition is an anticipated outcome of probiotic supplementation, the extent to which PS128 improved intestinal architecture and barrier-associated features in *Fmr1* KO mice was less certain and therefore warrants further consideration. Consistent with this observation, PS128 ameliorated gastrointestinal abnormalities and barrier-associated features, suggesting that stabilization of microbial ecology may contribute to improved intestinal structural integrity.[30] In addition, PS128 increased the abundance of *Lactiplantibacillus paraplantarum*, *Levilactobacillus brevis*, and *Bifidobacterium pseudolongum*. Notably, *Lactiplantibacillus paraplantarum* has been reported to improve diabetes-related gastrointestinal complications and exert anti-inflammatory effects.[31,32] Together, these observations support a psychobiotic mode of action in which PS128 promotes gut microbial homeostasis and intestinal integrity.[15,16,33]

Beyond compositional rearrangement, PS128 produced a distinct functional correction centered on the arginine–ornithine–polyamine metabolic pathway. Because PS128 lacks de novo putrescine biosynthesis but encodes uptake and catabolic functions, it likely contributes to the regulation of systemic putrescine handling rather than serving as a primary source of polyamine production. Consistent with this role, PS128 normalized the elevated prefrontal cortex (PFC)-to-serum putrescine ratio in *Fmr1* KO mice toward wild-type levels. This correction was accompanied by reduced expression of the polyamine transporters ATP13A2 and ATP13A3 in the PFC, together with decreased *Atp13a4* expression in astrocytes at the single-cell level in PS128-treated *Fmr1* KO mice. ATP13A2 and ATP13A3 are major determinants of

mammalian polyamine uptake,[34] and their downregulation is consistent with reduced prefrontal cortical accumulation of putrescine. Mutations or dysfunction in these transporters have been associated with ASD and related neurodevelopmental conditions.[35-39] Together, these observations link microbial activity to central polyamine handling and support a model in which PS128 modulates gut-derived putrescine flux and neuronal transporter expression.

We identify putrescine as a microbiota-sensitive modulator of autism-like behaviors. Elevating peripheral putrescine was sufficient to induce anxiety-like behaviors, social impairments, and motor deficits in wild-type mice, whereas inhibition of endogenous putrescine synthesis with DFMO ameliorated these abnormalities in *Fmr1* KO mice. At physiological pH, putrescine carries a positive charge and interacts with nucleic acids, phospholipids, and anionic proteins, thereby influencing macromolecular conformation, autophagy, membrane dynamics, and inflammatory signaling. Altered polyamine handling, including astrocytic uptake via ATP13A4, has been shown to tune excitatory synaptic transmission and neuronal physiology.[40] Because putrescine serves as a metabolic precursor for astrocyte-derived γ-aminobutyric acid (GABA) through a noncanonical MAO-B- and ALDH-dependent pathway,[41] perturbations in putrescine availability may reshape inhibitory tone and excitation–inhibition balance in cortical circuits. Clinical observations of elevated salivary putrescine[13] and increased activity of the gut microbial arginine–polyamine program in children with ASD[42] further support the concept that putrescine delineates a metabolically defined ASD subtype that may be particularly responsive to psychobiotic interventions such as PS128.

In our study, initiating DFMO at four weeks of age raised safety considerations, as juvenile *Fmr1* KO mice already exhibited mild anxiety-like behaviors. These results suggest that early inhibition of endogenous putrescine synthesis may exert age-dependent adverse effects on emotional regulation. Across behavioral endpoints, PS128 produced broader and more consistent improvements than DFMO, consistent with its combined ecological (microbiota restructuring) and metabolic (polyamine modulation) actions.

Probiotic-based approaches are increasingly recognized as safe, non-pharmacological options for neurological and psychiatric disorders. *Lactobacillus reuteri* restored social behavior through vagus-dependent oxytocinergic and dopaminergic signaling.[43] The microbial metabolite 5-aminovaleric acid improved autism-like behaviors in BTBR mice by reducing pyramidal neuron excitability in the PFC.[29] *Bacteroides uniformis* reinstated excitation–inhibition balance in *Chd8*$^{+/-}$ mice by modulating intestinal amino acid transport and reducing prefrontal glutamine levels.[44] In a valproic acid–induced ASD mouse model, PS128 ameliorated social and memory deficits by enhancing oxytocin signaling and increasing dendritic complexity in the hippocampus and PFC.[45] Collectively, these studies support a framework in which psychobiotics act at the interface of microbial metabolites, host transport systems, and cortical circuit function. As metabolic abnormalities have been widely reported in ASD across multiple metabolomics studies, we suggest that future diagnostic strategies may complement current behavior-based diagnostic approaches (e.g., clinical assessments based on DSM-5-TR) with metabolite-based stratification.

In conclusion, our findings identify putrescine as a potential metabolic marker of an ASD subtype and support a model in which PS128 modulates gut-derived polyamine metabolism and central transporter expression to restore social and stereotypic behaviors.

## Limitations of the study

This study has several limitations. We relied on a single genetic model, which limits the generalizability of our findings to other ASD subtypes. Although our multi-omics analyses support a gut-driven influence on central polyamine homeostasis, the specific contributions of individual transporters and brain cell types remain to be delineated. Future studies incorporating transporter-specific perturbations, isotope-labeled tracing of gut-to-brain polyamine flux, and in vivo circuit measurements during behavior will help clarify mechanistic causality. Clinical translation will also require longitudinal studies integrating microbiome, metabolomic, and behavioral profiling in human cohorts. Ultimately, PS128 may be combined with

pharmacological or behavioral interventions and tailored to baseline metabolic phenotypes, enabling precision treatment strategies for ASD subtypes characterized by disrupted arginine–ornithine–polyamine metabolism.

## RESOURCE AVAILABILITY

### *Lead contact*

Further information and requests for resources and reagents should be directed to and will be fulfilled by the lead contact, Yi-Hsuan Pan (yxpan@sat.ecnu.edu.cn).

### *Materials availability*

This study did not generate new unique reagents. All materials generated in this study are available from the lead contact with a completed material transfer agreement.

### *Data and code availability*

- Whole-genome sequencing data for *Lactiplantibacillus plantarum* PS128 have been deposited in NCBI-SRA under accession number PRJNA1345344.
- 16S rRNA sequencing data have been deposited in NCBI-SRA under accession number PRJNA1345244.
- Metagenomic sequencing data have been deposited in NCBI-SRA under accession number PRJNA1345245.
- Single-nucleus RNA sequencing data have been deposited in NCBI-SRA under accession number PRJNA1345209.
- This paper does not report original code.
- Any additional information required to reanalyze the data reported in this paper is available from the lead contact upon request.

## ACKNOWLEDGMENTS

This work was supported by the National Natural Science Foundation of China (grant numbers 31100273 to Y.H.P. and 81941013 and 32271022 to X.B.Y.); the Key Laboratory of Brain Functional Genomics at East China Normal University (grant number 23SKBFGK2 to Y.H.P. and H.L.); the National Key Research and Development Program of China (grant number 2022YFC2705200); the National Natural Science Foundation of China–Israel Science Foundation Cooperative Research Project (grant number 32061143016); and the Fundamental Research Funds for the Central Universities.

## AUTHOR CONTRIBUTIONS

Y.H.P. and X.B.Y. conceived and supervised the project and obtained funding. Y.M.C., Y.X.C., and S.Z. conducted behavioral, histological, and molecular analyses. J.L.C., Y.X.C., Y.M.C., T.A.L., and S.S.G. conducted data processing. Y.M.C., Y.X.C., and Y.H.P. conducted data analysis and figure organization. Y.H.P., X.B.Y., Y.C.T., Y.W.L., J.M., W.Z., and H.P.L. contributed to the discussion and data interpretation. Y.M.C., Y.X.C., Y.H.P., and X.B.Y. wrote the manuscript. All authors read and approved the final manuscript.

## DECLARATION OF INTERESTS

The authors declare no competing interests.

## DECLARATION OF GENERATIVE AI AND AI-ASSISTED TECHNOLOGIES

During the preparation of this work, the author(s) used ChatGPT 5.2 in order to check the grammatical errors of the paper. After using this tool/service, the author(s) reviewed and edited the content as needed and take(s) full responsibility for the content of the published article.

## SUPPLEMENTAL INFORMATION

Document S1. Figures S1–S7
Table S1. Raw data related to Figures 1–6.
Table S2. Raw data related to Figures S1–S7.
Video S1. Voluntary intake of PS128-containing or blank jelly in mice.
Video S2. Behavioral statistics from the olfactory habituation/dishabituation test, related to Figure S1.
Video S3. Four specific behaviors in the olfactory habituation/dishabituation test, related to Figure S1.

## FIGURE TITLES AND LEGENDS

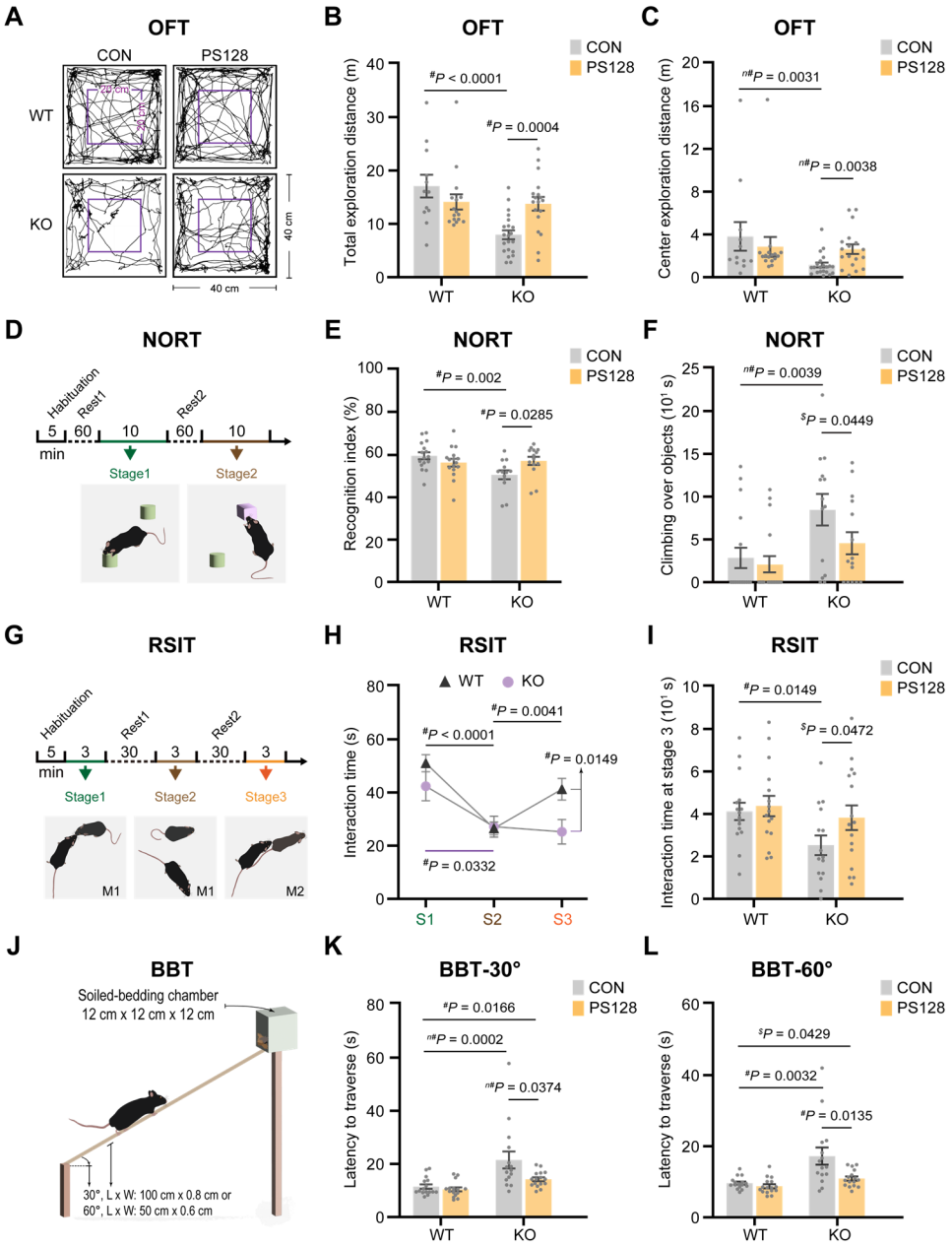


**Figure 1. PS128 supplementation mitigates autism-like behaviors in *Fmr1* KO mice**

(A–C) Representative traces in the open-field test (OFT) (A), total exploration distance (B), and center exploration distance (C), $n$ = 12–21.

(D–F) Schematic of the novel object recognition test (NORT) (D), recognition index (%) = (novel) / (novel + familiar) x 100, based on sniffing time (E), and total time spent climbing over objects (F), $n$ = 13–18.

(G–I) Schematic of the reciprocal social interaction test (RSIT) (G), interaction time with familiar or novel mice across three stages (H), and interaction time at Stage 3 (I), $n$ = 15–16. S, stage.

(J–L) Schematic of the balance beam test (BBT) (J), latency to traverse a 30° beam (K), or a 60° beam (L), $n$ = 15–16. Data are presented as mean ± S.E.M. and gray dots indicate individual mice. One-tailed ($^{\$}$) or

two-tailed ([#]) Student's *t*-test and two-tailed ([n#]) Mann–Whitney U test were used where appropriate. A *P* value < 0.05 was considered statistically significant.
See also Figure S1.

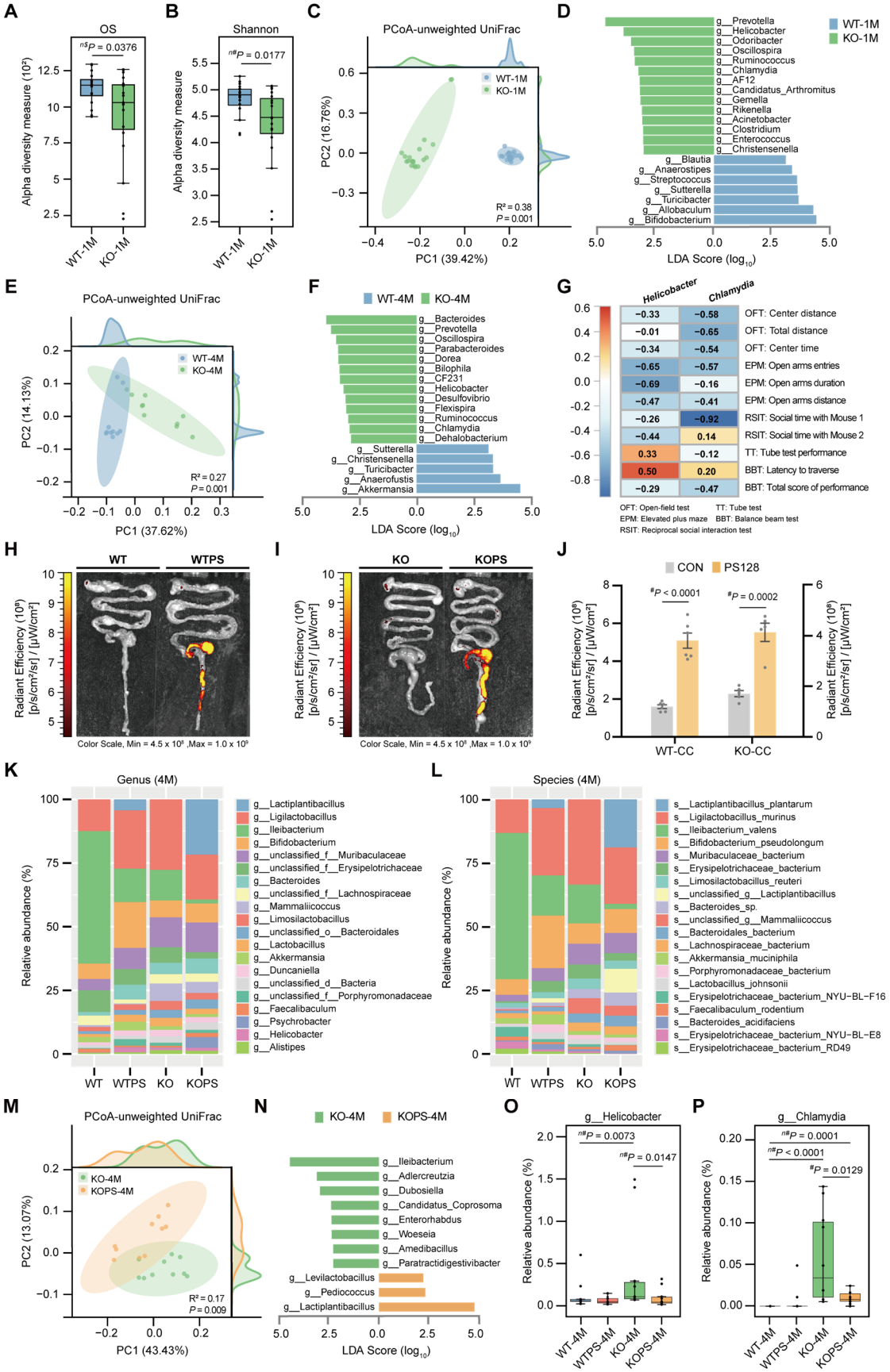
A
OS
n$P = 0.0376
Alpha diversity measure (10²)
WT-1M
KO-1M
B
Shannon
n#P = 0.0177
Alpha diversity measure
C
PCoA-unweighted UniFrac
WT-1M
KO-1M
PC2 (16.76%)
PC1 (39.42%)
R² = 0.38
P = 0.001
D
WT-1M
KO-1M
g__Prevotella
g__Helicobacter
g__Odoribacter
g__Oscillospira
g__Ruminococcus
g__Chlamydia
g__AF12
g__Candidatus_Arthromitus
g__Gemella
g__Rikenella
g__Acinetobacter
g__Clostridium
g__Enterococcus
g__Christensenella
g__Blautia
g__Anaerostipes
g__Streptococcus
g__Sutterella
g__Turicibacter
g__Allobaculum
g__Bifidobacterium
LDA Score (log10)
E
PCoA-unweighted UniFrac
WT-4M
KO-4M
PC2 (14.13%)
PC1 (37.62%)
R² = 0.27
P = 0.001
F
WT-4M
KO-4M
g__Bacteroides
g__Prevotella
g__Oscillospira
g__Parabacteroides
g__Dorea
g__Bilophila
g__CF231
g__Helicobacter
g__Desulfovibrio
g__Flexispira
g__Ruminococcus
g__Chlamydia
g__Dehalobacterium
g__Sutterella
g__Christensenella
g__Turicibacter
g__Anaerofustis
g__Akkermansia
LDA Score (log10)
G
Helicobacter
Chlamydia
OFT: Center distance −0.33 −0.58
OFT: Total distance −0.01 −0.65
OFT: Center time −0.34 −0.54
EPM: Open arms entries −0.65 −0.57
EPM: Open arms duration −0.69 −0.16
EPM: Open arms distance −0.47 −0.41
RSIT: Social time with Mouse 1 −0.26 −0.92
RSIT: Social time with Mouse 2 −0.44 0.14
TT: Tube test performance 0.33 −0.12
BBT: Latency to traverse 0.50 0.20
BBT: Total score of performance −0.29 −0.47
OFT: Open-field test
TT: Tube test
EPM: Elevated plus maze
BBT: Balance beam test
RSIT: Reciprocal social interaction test
H
WT
WTPS
Radiant Efficiency (10⁸) [p/s/cm²/sr] / [μW/cm²]
Color Scale, Min = 4.5 x 10⁸ ,Max = 1.0 x 10⁹
I
KO
KOPS
Radiant Efficiency (10⁸) [p/s/cm²/sr] / [μW/cm²]
Color Scale, Min = 4.5 x 10⁸ ,Max = 1.0 x 10⁹
J
CON
PS128
#P < 0.0001
#P = 0.0002
Radiant Efficiency (10⁸) [p/s/cm²/sr] / [μW/cm²]
WT-CC
KO-CC
K
Genus (4M)
Relative abundance (%)
g__Lactiplantibacillus
g__Ligilactobacillus
g__Ileibacterium
g__Bifidobacterium
g__unclassified_f__Muribaculaceae
g__unclassified_f__Erysipelotrichaceae
g__Bacteroides
g__unclassified_f__Lachnospiraceae
g__Mammaliicoccus
g__Limosilactobacillus
g__unclassified_o__Bacteroidales
g__Lactobacillus
g__Akkermansia
g__Duncaniella
g__unclassified_d__Bacteria
g__unclassified_f__Porphyromonadaceae
g__Faecalibaculum
g__Psychrobacter
g__Helicobacter
g__Alistipes
WT
WTPS
KO
KOPS
L
Species (4M)
Relative abundance (%)
s__Lactiplantibacillus_plantarum
s__Ligilactobacillus_murinus
s__Ileibacterium_valens
s__Bifidobacterium_pseudolongum
s__Muribaculaceae_bacterium
s__Erysipelotrichaceae_bacterium
s__Limosilactobacillus_reuteri
s__unclassified_g__Lactiplantibacillus
s__Bacteroides_sp.
s__unclassified_g__Mammaliicoccus
s__Bacteroidales_bacterium
s__Lachnospiraceae_bacterium
s__Akkermansia_muciniphila
s__Porphyromonadaceae_bacterium
s__Lactobacillus_johnsonii
s__Erysipelotrichaceae_bacterium_NYU−BL−F16
s__Faecalibaculum_rodentium
s__Bacteroides_acidifaciens
s__Erysipelotrichaceae_bacterium_NYU−BL−E8
s__Erysipelotrichaceae_bacterium_RD49
WT
WTPS
KO
KOPS
M
PCoA-unweighted UniFrac
KO-4M
KOPS-4M
PC2 (13.07%)
PC1 (43.43%)
R² = 0.17
P = 0.009
N
KO-4M
KOPS-4M
g__Ileibacterium
g__Adlercreutzia
g__Dubosiella
g__Candidatus_Coprosoma
g__Enterorhabdus
g__Woeseia
g__Amedibacillus
g__Paratractidigestivibacter
g__Levilactobacillus
g__Pediococcus
g__Lactiplantibacillus
LDA Score (log10)
O
g__Helicobacter
n#P = 0.0073
n#P = 0.0147
Relative abundance (%)
WT-4M
WTPS-4M
KO-4M
KOPS-4M
P
g__Chlamydia
n#P = 0.0001
n#P < 0.0001
#P = 0.0129
Relative abundance (%)
WT-4M
WTPS-4M
KO-4M
KOPS-4M

401

**Figure 2. Gut microbiota diversity, community structure, and taxonomic changes in mice with or without PS128 treatment.**

(A–D) Gut microbiota analysis of 1-month-old *Fmr1* KO mice and their wild-type (WT) littermates without PS128 intervention. Observed species (A). Shannon diversity index (B). Principal coordinates analysis (PCoA) plot based on unweighted UniFrac distances (C). Histogram of linear discriminant analysis (LDA) scores from LEfSe analysis at the genus level, logarithmic LDA score cutoff > 3.0, $P < 0.05$ (D), $n = 19–20$.

(E and F) Gut microbiota analysis of 4-month-old *Fmr1* KO mice and their WT littermates following 3 months of PS128 supplementation. PCoA plot (E). Histogram of logarithmic LDA scores, cutoff > 2.5, $P < 0.05$ (F), $n = 10$.

(G) Spearman's rank correlation analysis between the relative abundance of *Helicobacter* and *Chlamydia* and behavioral performance in 4-month-old *Fmr1* KO mice, $n = 10–11$.

(H–J) Biodistribution of PS128 in the gastrointestinal tract. Representative ex vivo fluorescence images of the gut from *Fmr1* KO mice and their WT littermates after oral gavage with fluorescently labeled PS128 (H and I). Average radiant efficiency quantified from the cecum and colon (CC) (J), $n = 5–6$.

(K and L) Relative abundance of gut microbiota at the genus (K) and species (L) levels in 4-month-old groups, $n = 11–13$.

(M and N) Gut microbiota analysis comparing 4-month-old *Fmr1* KO mice with or without PS128 treatment (KO or KOPS). PCoA plot (M). Histogram of logarithmic LDA scores, cutoff > 2.2, $P < 0.05$ (N), $n = 10-11$.

(O and P) Relative abundance of *Helicobacter* (O) and *Chlamydia* (P) across 4-month-old groups, $n = 10$.

Data are presented as mean ± S.E.M. and each dot represents an individual mouse. Statistical significance was determined by two-tailed Student's *t*-test ($^{\#}$), one-tailed ($^{n\$}$), or two-tailed ($^{n\#}$) Mann–Whitney U test, as appropriate. A $P$ value < 0.05 was considered significant.

See also Figures S2 and S3.

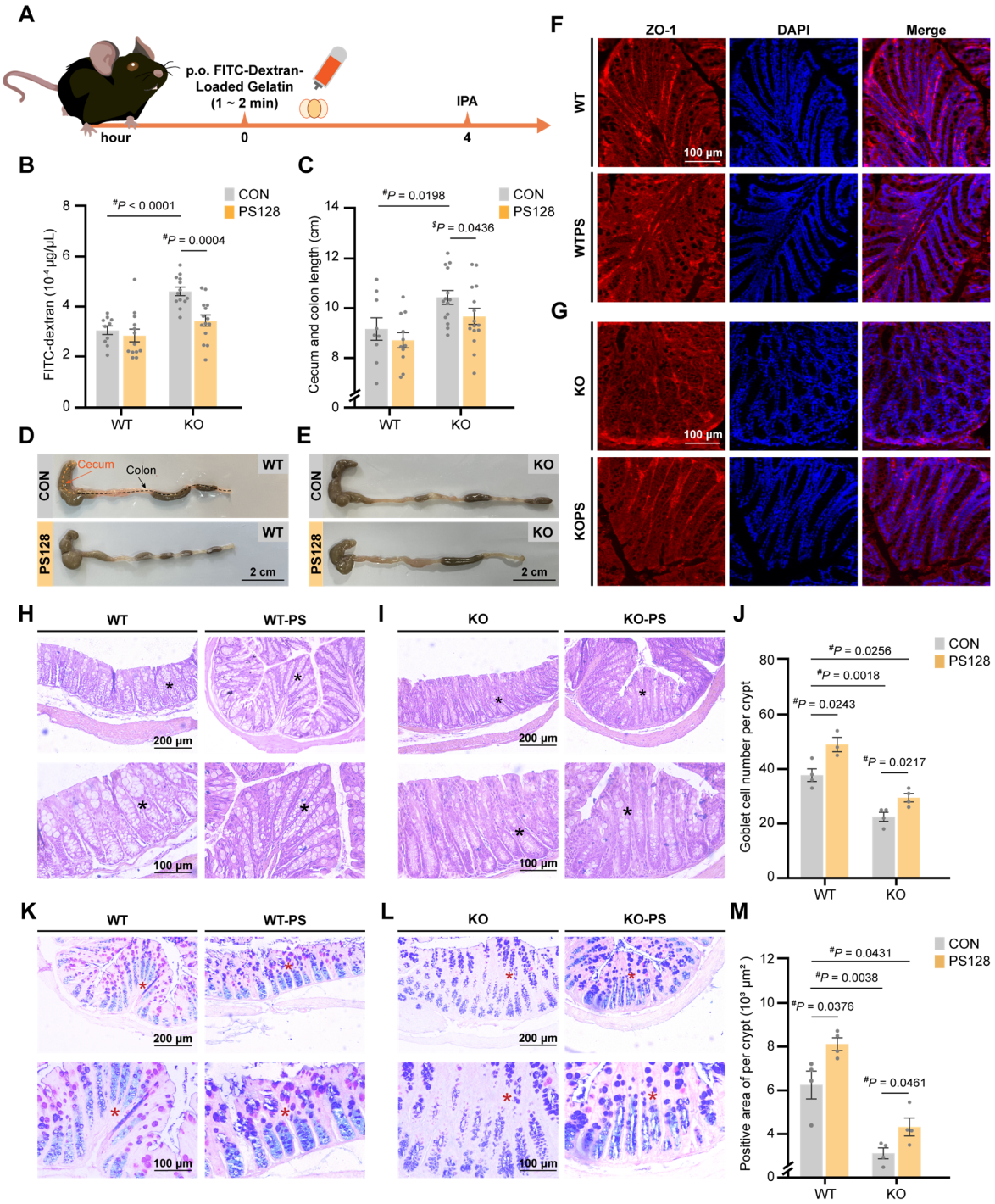


425

426 **Figure 3. PS128 restores gut barrier function and integrity in *Fmr1* KO mice**

427 (A and B) Assessment of intestinal permeability. Schematic of intestinal permeability assay (IPA) (A). Serum
428 FITC-dextran concentrations after orally self-consumed FITC–dextran–loaded gelatin (B), $n$ = 10–14.
429 (C–E) Gross anatomical assessment of the large intestine. Average length of the cecum and colon, $n$ = 9–
430 15 (C). Representative images of dissected tissues (D and E).
431 (F and G) Colon integrity. Representative immunofluorescence images of colonic sections stained for ZO-
432 1 (red) and nuclei (DAPI, blue). Scale bar, 100 μm.

433 (H–J) Histological evaluation of colonic architecture. Representative H&E–stained sections of *Fmr1* KO and
434 their WT littermates with/without PS128 intervention (H and I). Quantification of goblet cells per crypt
435 (average of 3 crypts per section, 3 sections per mouse), $n$ = 3–4 (J). Scale bars, 200 μm and 100 μm.
436 (K–M) Analysis of mucin production. Representative AB–PAS–stained sections showing acidic and neutral
437 mucins in blue and magenta for KO and their WT littermates with/without PS128 intervention (K and L).
438 Quantification of MUC2-positive light blue and dark purple areas per crypt, 3 crypts per mouse, $n$ = 4 (M).
439 Scale bars, 200 μm and 100 μm. Data are mean ± S.E.M. and each dot represents an individual mouse.
440 Statistical significance was determined by one-tailed ($^{\$}$) or two-tailed ($^{\#}$) Student's $t$-test. A $P$ value < 0.05
441 was considered significant.

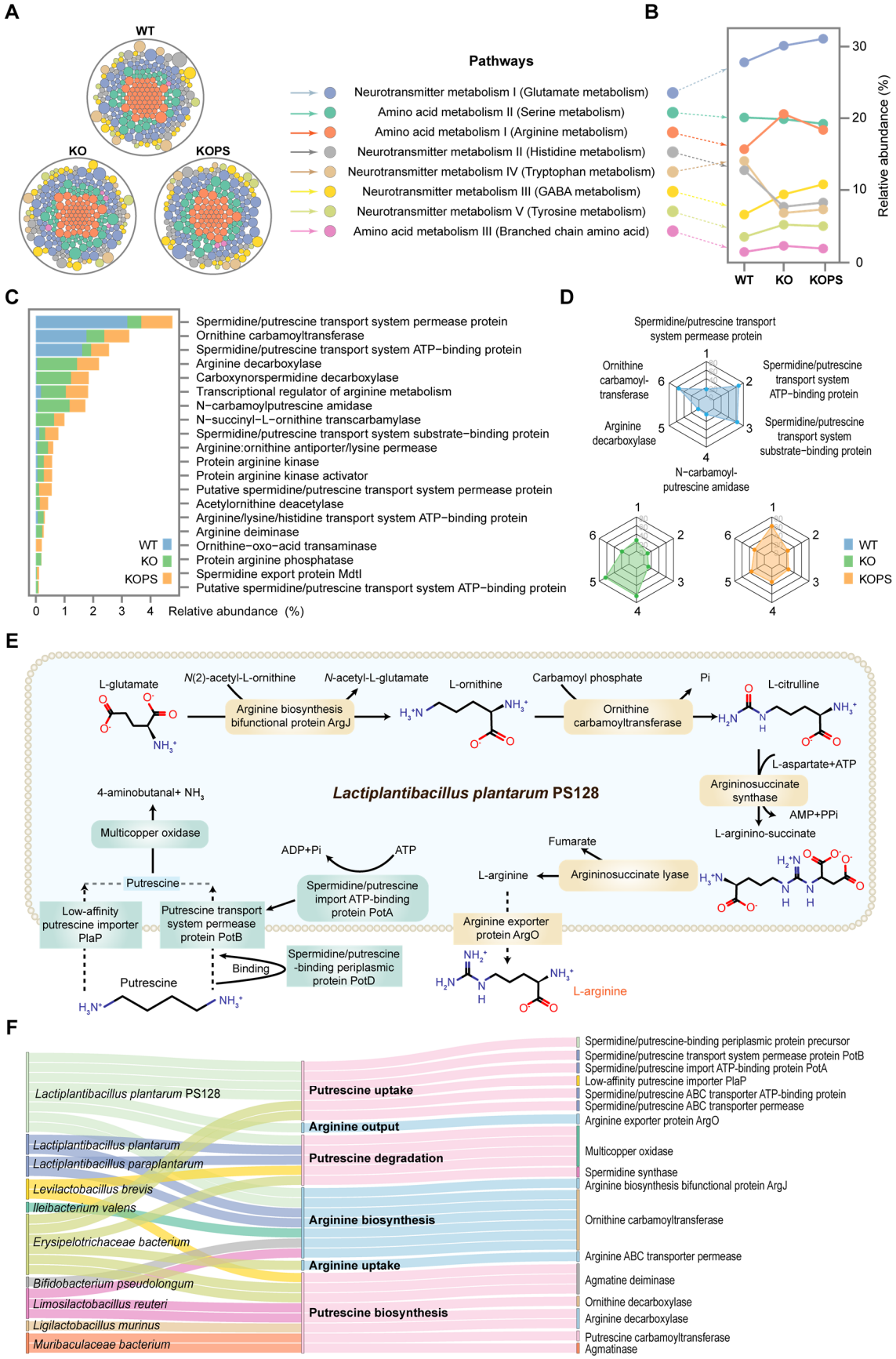
A
WT
KO
KOPS
Pathways
Neurotransmitter metabolism I (Glutamate metabolism)
Amino acid metabolism II (Serine metabolism)
Amino acid metabolism I (Arginine metabolism)
Neurotransmitter metabolism II (Histidine metabolism)
Neurotransmitter metabolism IV (Tryptophan metabolism)
Neurotransmitter metabolism III (GABA metabolism)
Neurotransmitter metabolism V (Tyrosine metabolism)
Amino acid metabolism III (Branched chain amino acid)
B
Relative abundance (%)
WT KO KOPS
C
Spermidine/putrescine transport system permease protein
Ornithine carbamoyltransferase
Spermidine/putrescine transport system ATP−binding protein
Arginine decarboxylase
Carboxynorspermidine decarboxylase
Transcriptional regulator of arginine metabolism
N−carbamoylputrescine amidase
N−succinyl−L−ornithine transcarbamylase
Spermidine/putrescine transport system substrate−binding protein
Arginine:ornithine antiporter/lysine permease
Protein arginine kinase
Protein arginine kinase activator
Putative spermidine/putrescine transport system permease protein
Acetylornithine deacetylase
Arginine/lysine/histidine transport system ATP−binding protein
Arginine deiminase
Ornithine−oxo−acid transaminase
Protein arginine phosphatase
Spermidine export protein MdtI
Putative spermidine/putrescine transport system ATP−binding protein
Relative abundance (%)
D
E
L-glutamate
N(2)-acetyl-L-ornithine
N-acetyl-L-glutamate
Arginine biosynthesis bifunctional protein ArgJ
L-ornithine
Carbamoyl phosphate
Ornithine carbamoyltransferase
Pi
L-citrulline
L-aspartate+ATP
Argininosuccinate synthase
AMP+PPi
L-arginino-succinate
Lactiplantibacillus plantarum PS128
4-aminobutanal+ NH3
Multicopper oxidase
Putrescine
ADP+Pi
ATP
Spermidine/putrescine import ATP-binding protein PotA
Fumarate
L-arginine
Argininosuccinate lyase
Low-affinity putrescine importer PlaP
Putrescine transport system permease protein PotB
Arginine exporter protein ArgO
Binding
Spermidine/putrescine -binding periplasmic protein PotD
Putrescine
L-arginine
F
Lactiplantibacillus plantarum PS128
Lactiplantibacillus plantarum
Lactiplantibacillus paraplantarum
Levilactobacillus brevis
Ileibacterium valens
Erysipelotrichaceae bacterium
Bifidobacterium pseudolongum
Limosilactobacillus reuteri
Ligilactobacillus murinus
Muribaculaceae bacterium
Putrescine uptake
Arginine output
Putrescine degradation
Arginine biosynthesis
Arginine uptake
Putrescine biosynthesis
Spermidine/putrescine-binding periplasmic protein precursor
Spermidine/putrescine transport system permease protein PotB
Spermidine/putrescine import ATP-binding protein PotA
Low-affinity putrescine importer PlaP
Spermidine/putrescine ABC transporter ATP-binding protein
Spermidine/putrescine ABC transporter permease
Arginine exporter protein ArgO
Multicopper oxidase
Spermidine synthase
Arginine biosynthesis bifunctional protein ArgJ
Ornithine carbamoyltransferase
Arginine ABC transporter permease
Agmatine deiminase
Ornithine decarboxylase
Arginine decarboxylase
Putrescine carbamoyltransferase
Agmatinase

442

443 **Figure 4. PS128 modulates gut microbial arginine–ornithine–polyamine metabolism in *Fmr1* KO**
444 **mice**
445 (A–D) Distribution of gut–brain modules (GBMs) at the species level. Each GBM is represented by a distinct
446 color (A). GBMs were classified into eight functional clusters based on their association with gut–brain
447 metabolic pathways. Relative abundance (%) of total modules within each GBM cluster (B). Relative
448 abundance (%) of proteins encoded by bins related to "Amino acid metabolism I" (C). Key pathways in
449 amine metabolism within "Amino acid metabolism I" (D). $n$ = 11–13 per group.
450 (E) Schematic of metabolic pathways annotated from whole-genome sequencing of PS128.
451 (F) Sankey diagram showing correlations between genes encoding enzymes involved in arginine, ornithine,
452 and spermidine/putrescine metabolism and bacterial strains enriched by PS128, together with the six most
453 abundant bacterial species.
454 See also Figure S4.
455

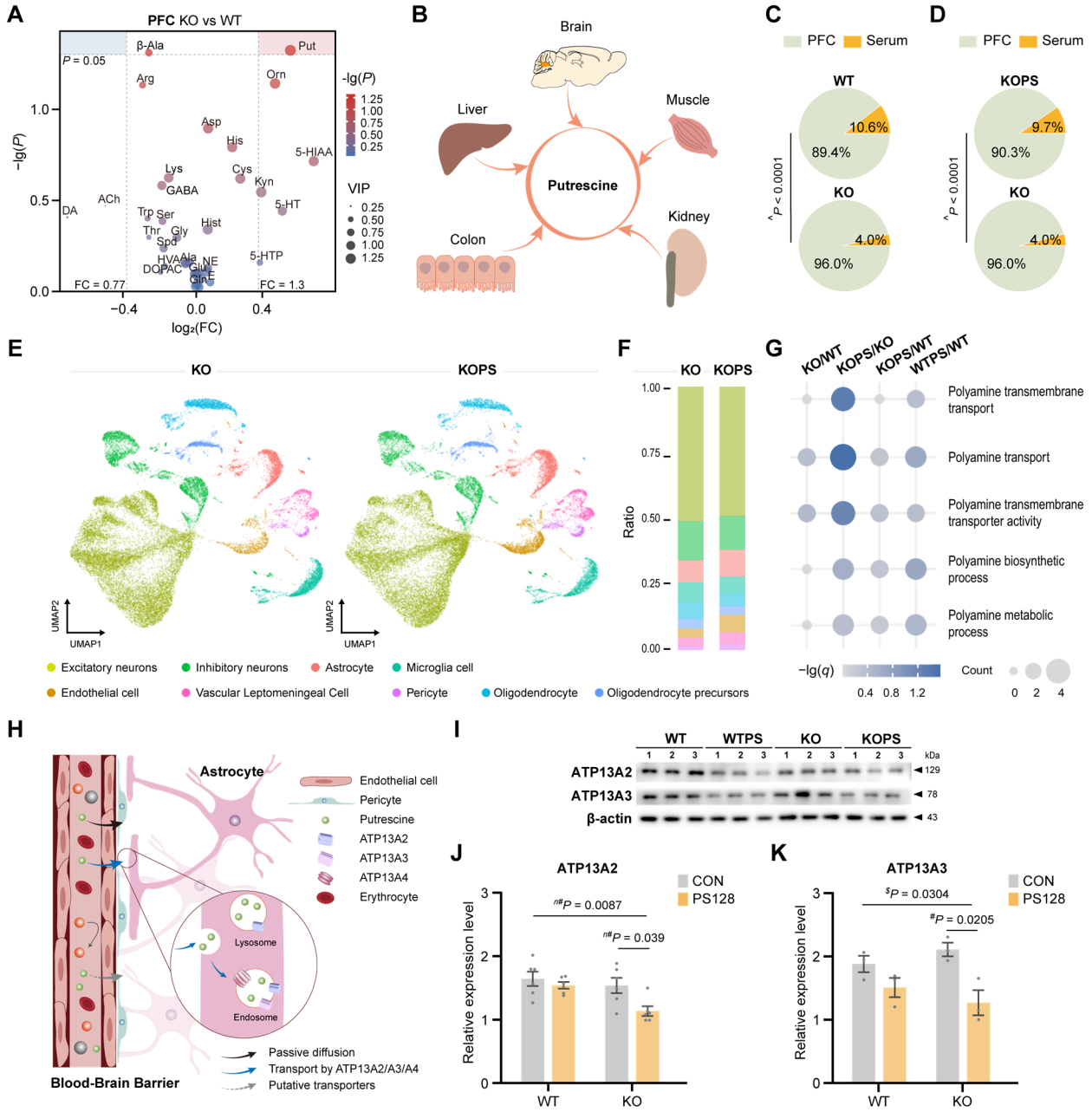


**Figure 5. PS128 restores PFC–serum putrescine balance and reduces putrescine transporter expression in *Fmr1* KO mice**

(A) Differential metabolites in the PFC between KO and WT mice. Colors indicate -$\log_{10}$(*P* value), and bubble sizes represent variable importance in projection (VIP) scores. The x-axis denotes $\log_2$(fold change). *n* = 3 biological replicates, each pooled from six individuals (18 mice per group). FC, fold change.

(B) Schematic illustrating major peripheral organs as sources of circulating putrescine.

(C and D) Ratios of putrescine in the PFC relative to serum in WT versus KO mice (C) and in KOPS versus KO mice (D). *n* = 6 mice per group.

(E and F) UMAP projection (E) and stacked bar plots (F) of cell-type composition derived from single-nucleus RNA sequencing (snRNA-seq) of PFC from 15-week-old mice. *n* = 2 biological replicates per group, each pooled from 3–4 individuals (7–8 mice per group).

(G) Gene Ontology (GO) enrichment of differentially expressed genes (DEGs) in the PFC, highlighting pathways related to polyamine transport. $-\log_{10}(q \text{ value}) > 1.3$ was considered significant. Count, number of DEGs. DEGs were defined as $P < 0.05$ and $|\log_2 \text{ fold change}| \geq 0.12$ with expression in at least 10% of PFC cells (Methods).

(H) Schematic of two principal routes for putrescine transport. Putrescine crosses the blood–brain barrier (BBB) by passive diffusion or via active transport mediated by P5B-type ATPases (ATP13A2, ATP13A3, ATP13A4) and other putative transporters.

(I–K) Western blot of ATP13A2, ATP13A3, and β-actin in the PFC (I), with densitometric quantification of ATP13A2 (J) and ATP13A3 (K) normalized to β-actin. $n$ = 3–6 mice per group. Data are presented as mean ± S.E.M. and gray dot represents individual mice. Statistical significance was determined using one-tailed ($^{\$}$) or two-tailed ($^{\#}$) Student's $t$-test, or two-tailed ($^{n\#}$) Mann–Whitney U test as appropriate. A chi-square (^) test was used in (C and D). A $P$ value < 0.05 was considered significant.

See also Figures S5 and S6.

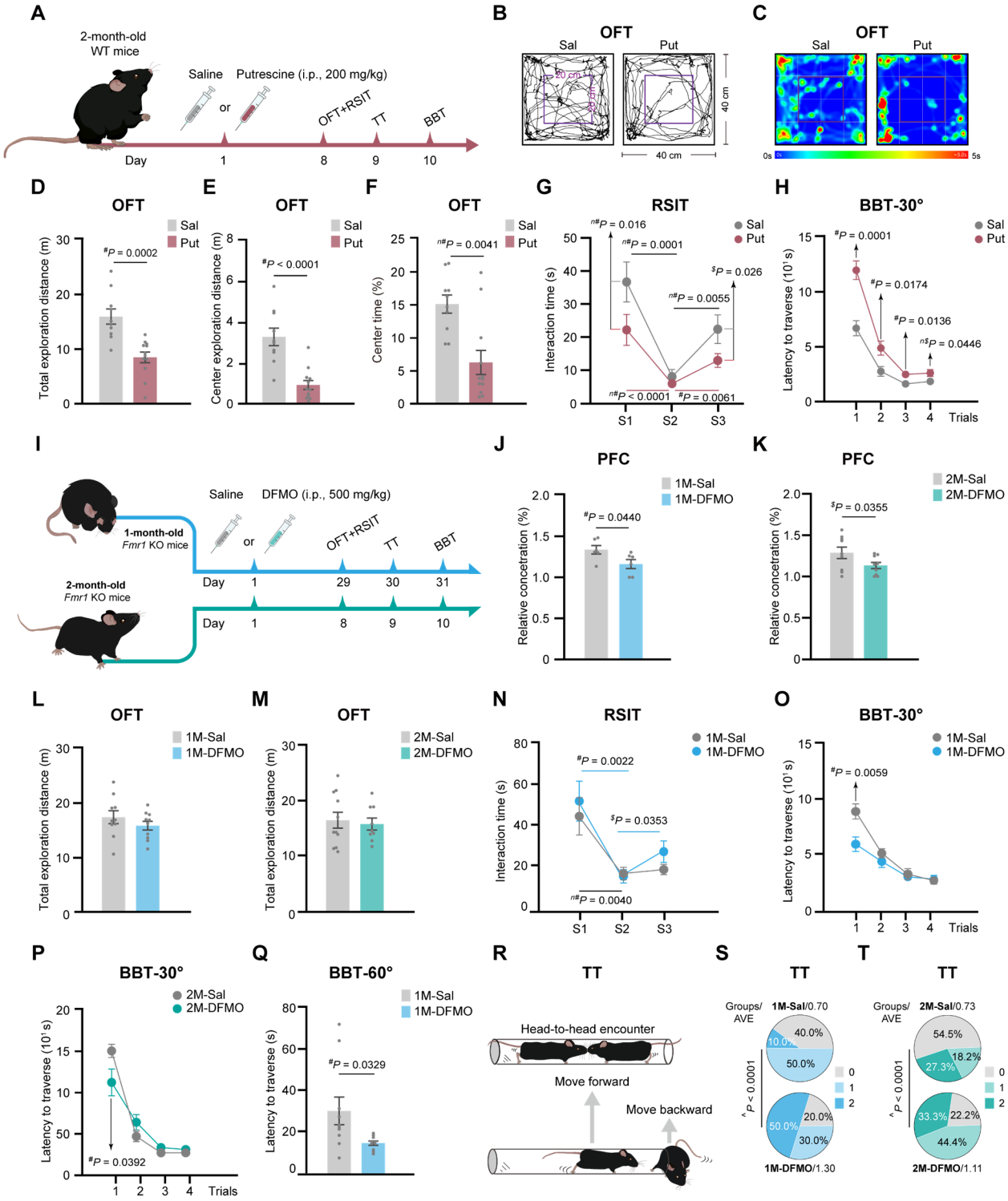


481

482 **Figure 6. Putrescine imbalance modulates autism-like behaviors in mice**

483 (A) Schematic of putrescine intervention in 2-month-old WT mice and behavioral tests. i.p., intraperitoneal
484 injection.

485 (B–F) Representative traces (B) and heatmap (C) of the open-field test (OFT), total exploration distance
486 (D), center exploration distance (E), and time spent in the center area (F).

(G) Interaction time with familiar or novel mice across three stages of the reciprocal social interaction test (RSIT). S, stage.

(H) Latency to traverse a 30° beam across four trials of the balance beam test (BBT). Effects of exogenous putrescine intervention in 2-month-old WT mice (B–H), $n$ = 10–12.

(I) Schematic of DFMO intervention in 1- or 2-month-old *Fmr1* KO mice. i.p., intraperitoneal injection.

(J and K) Relative putrescine concentration in the PFC after DFMO or saline injection from 1 month (J) or 2 months (K) of age, $n$ = 6–9.

(L and M) Total exploration distance in the OFT.

(N) Interaction time with familiar or novel mice across three stages of the RSIT.

(O–Q) Latency to traverse a 30° beam across four trials (O and P) or a 60° beam (Q) of the BBT.

(R–T) Schematic of the tube test (TT) (R) and average score (AVE) per mouse obtained in the TT (S and T). Effects of endogenous putrescine inhibition by DFMO in 1- or 2-month-old *Fmr1* KO mice (J–T), $n$ = 9–11. Data are presented as mean ± S.E.M. and gray dots indicate individual mice. One-tailed ($^{\$}$) or two-tailed ($^{\#}$) Student's $t$-test, one-tailed ($^{n\$}$) or two-tailed ($^{n\#}$) Mann–Whitney U test were used as appropriate. A chi-square (^) test was used in (S and T). A $P$ value < 0.05 was considered significant.

See also Figure S7.

## REFERENCES


1. Cao, X.X., Jia, J.Y., Li, Z., Guo, S.M., Duan, J.L., Ma, J., Yuan, X.B., and Pan, Y.H. (2025). *Cadherin 11* regulates presynaptic vesicle trafficking and neuronal activity in autism-related brain circuit. Mol. Psychiatr., 17. 10.1038/s41380-025-03141-7.

2. Shaw, K.A., Bilder, D.A., McArthur, D., Williams, A.R., Amoakohene, E., Bakian, A.V., Durkin, M.S., Fitzgerald, R.T., Furnier, S.M., Hughes, M.M., et al. (2023). Early Identification of Autism Spectrum Disorder Among Children Aged 4 Years - Autism and Developmental Disabilities Monitoring Network, 11 Sites, United States, 2020. MMWR Surveill. Summ. *72*, 1-15. 10.15585/mmwr.ss7201a1.

3. Collaborators, G.B.o.D.S.A.S. (2025). The global epidemiology and health burden of the autism spectrum: findings from the Global Burden of Disease Study 2021. Lancet Psychiatry *12*, 111-121. 10.1016/s2215-0366(24)00363-8.

4. Pan, Y.H., Wu, N., and Yuan, X.B. (2019). Toward a Better Understanding of Neuronal Migration Deficits in Autism Spectrum Disorders. Front. Cell Dev. Biol. *7*, 205. 10.3389/fcell.2019.00205.

5. Tarlungeanu, D.C., Deliu, E., Dotter, C.P., Kara, M., Janiesch, P.C., Scalise, M., Galluccio, M., Tesulov, M., Morelli, E., Sonmez, F.M., et al. (2016). Impaired Amino Acid Transport at the Blood Brain Barrier Is a Cause of Autism Spectrum Disorder. Cell *167*, 1481-1494. 10.1016/j.cell.2016.11.013.

6. Liu, A., Zhou, W., Qu, L., He, F., Wang, H., Wang, Y., Cai, C., Li, X., Zhou, W., and Wang, M. (2019). Altered Urinary Amino Acids in Children With Autism Spectrum Disorders. Front. Cell. Neurosci. *13*, 7. 10.3389/fncel.2019.00007.

7. Wang, L., Zheng, R., Xu, Y., Zhou, Z., Guan, P., Wu, Y., Zhou, J., Cheng, Z., and Zhang, L. (2022). Altered Metabolic Characteristics in Plasma of Young Boys with Autism Spectrum Disorder. Journal of Autism and Developmental Disorders *52*, 4897-4907. 10.1007/s10803-021-05364-3.

8. Wang, M., Liang, Z., Zhuang, H., Cao, X., Ma, G., Sun, Y., Yan, X., Ran, X., Guan, H., and Shen, L. (2025). *Cntn4* Gene Deficiency Promotes Autism-Like Phenotypes Associated with Gut Microbiota Perturbations and Gut-Brain Axis Metabolomic Alterations in Mice. Mol. Neurobiol. *63*, 235. 10.1007/s12035-025-05567-0.

9. Wang, P., Wu, P.-F., Wang, H.-J., Liao, F., Wang, F., and Chen, J.-G. (2023). Gut microbiome-derived ammonia modulates stress vulnerability in the host. Nature Metabolism *5*, 1986-2001. 10.1038/s42255-023-00909-5.

10. Needham, B.D., Funabashi, M., Adame, M.D., Wang, Z., Boktor, J.C., Haney, J., Wu, W.-L., Rabut, C., Ladinsky, M.S., Hwang, S.-J., et al. (2022). A gut-derived metabolite alters brain activity and anxiety behaviour in mice. Nature *602*, 647-653. 10.1038/s41586-022-04396-8.

11. Holbert, C.E., Cullen, M.T., Casero, R.A., and Stewart, T.M. (2022). Polyamines in cancer: integrating organismal metabolism and antitumour immunity. Nature Reviews Cancer *22*, 467-480. 10.1038/s41568-022-00473-2.

12. Vrijsen, S., Houdou, M., Cascalho, A., Eggermont, J., and Vangheluwe, P. (2023). Polyamines in Parkinson's Disease: Balancing Between Neurotoxicity and Neuroprotection. Annu. Rev. Biochem. *92*, 435-464. 10.1146/annurev-biochem-071322-021330.

13. Siani-Rose, M., Cox, S., Goldstein, B., Abrams, D., Taylor, M., and Kurek, I. (2023). Cannabis-Responsive Biomarkers: A Pharmacometabolomics-Based Application to Evaluate the Impact of Medical Cannabis Treatment on Children with Autism Spectrum Disorder. Cannabis Cannabinoid Res. *8*, 126-137. 10.1089/can.2021.0129.

14. Snigdha, S., Ha, K., Tsai, P., Dinan, T.G., Bartos, J.D., and Shahid, M. (2022). Probiotics: Potential novel therapeutics for microbiota-gut-brain axis dysfunction across gender and lifespan. Pharmacol. Ther. *231*, 107978. 10.1016/j.pharmthera.2021.107978.

15. Liu, Y.W., Liong, M.T., Chung, Y.E., Huang, H.Y., Peng, W.S., Cheng, Y.F., Lin, Y.S., Wu, Y.Y., and Tsai, Y.C. (2019). Effects of *Lactobacillus plantarum* PS128 on Children with Autism Spectrum Disorder in Taiwan: A Randomized, Double-Blind, Placebo-Controlled Trial. Nutrients *11*, 820. 10.3390/nu11040820.

16. Mensi, M.M., Rogantini, C., Marchesi, M., Borgatti, R., and Chiappedi, M. (2021). *Lactobacillus plantarum* PS128 and Other Probiotics in Children and Adolescents with Autism Spectrum Disorder: A Real-World Experience. Nutrients *13*, 2036. 10.3390/nu13062036.

17. Gantois, I., Khoutorsky, A., Popic, J., Aguilar-Valles, A., Freemantle, E., Cao, R., Sharma, V., Pooters, T., Nagpal, A., Skalecka, A., et al. (2017). Metformin ameliorates core deficits in a mouse model of fragile X syndrome. Nat. Med. *23*, 674-677. 10.1038/nm.4335.

18. Protic, D.D., Aishworiya, R., Salcedo-Arellano, M.J., Tang, S.J., Milisavljevic, J., Mitrovic, F., Hagerman, R.J., and Budimirovic, D.B. (2022). Fragile X Syndrome: From Molecular Aspect to Clinical Treatment. Int. J. Mol. Sci. *23*, 1935. 10.3390/ijms23041935.

19. Guo, P.F., Yang, X.Y., Guo, X.M., Yang, H.E., Pan, J., and Li, Y. (2023). Dietary fish oil improves autistic behaviors and gut homeostasis by altering the gut microbial composition in a mouse model of fragile X syndrome. Brain Behav. Immun. *110*, 140-151. 10.1016/j.bbi.2023.02.019.

20. Goo, N., Bae, H.J., Park, K., Kim, J., Jeong, Y., Cai, M., Cho, K., Jung, S.Y., Kim, D.H., and Ryu, J.H. (2020). The effect of fecal microbiota transplantation on autistic-like behaviors in *Fmr1* KO mice. Life Sci. *262*, 10, 118497. 10.1016/j.lfs.2020.118497.

21. Cupolillo, D., Hoxha, E., Faralli, A., De Luca, A., Rossi, F., Tempia, F., and Carulli, D. (2016). Autistic-Like Traits and Cerebellar Dysfunction in Purkinje Cell *PTEN* Knock-Out Mice. Neuropsychopharmacology *41*, 1457-1466. 10.1038/npp.2015.339.

22. Holmberg, S.M., Feeney, R.H., Prasoodanan, P.K.V., Puértolas-Balint, F., Singh, D.K., Wongkuna, S., Zandbergen, L., Hauner, H., Brandl, B., Nieminen, A.I., et al. (2024). The gut commensal *Blautia* maintains colonic mucus function under low-fiber consumption through secretion of short-chain fatty acids. Nat. Commun. *15*, 3502. 10.1038/s41467-024-47594-w.

23. Gong, J., Chen, F., Jiang, B., Zhou, B., Ma, X., Wang, M., Dai, Q., Wang, S., Yang, X., and Zhao, E. (2025). Associations between blood systemic inflammatory markers and anxiety in *Helicobacter pylori*-infected patients. Front. Psychiatry *16*, 1671858. 10.3389/fpsyt.2025.1671858.

24. Hsu, T.W., Chu, C.S., Tsai, S.J., Bai, Y.M., Su, T.P., Chen, T.J., Chen, M.H., and Liang, C.S. (2022). Risk of Major Mental Disorder after Severe Bacterial Infections in Children and Adolescents: A Nationwide Longitudinal Study. Neuropsychobiology *81*, 539-549. 10.1159/000526984.

25. Valles-Colomer, M., Falony, G., Darzi, Y., Tigchelaar, E.F., Wang, J., Tito, R.Y., Schiweck, C., Kurilshikov, A., Joossens, M., Wijmenga, C., et al. (2019). The neuroactive potential of the human gut microbiota in quality of life and depression. Nature Microbiology *4*, 623-632. 10.1038/s41564-018-0337-x.

26. Agirman, G., and Hsiao, E.Y. (2021). SnapShot: The microbiota-gut-brain axis. Cell *184*, 2524-2524.e2521. 10.1016/j.cell.2021.03.022.

27. Needham, B.D., Adame, M.D., Serena, G., Rose, D.R., Preston, G.M., Conrad, M.C., Campbell, A.S., Donabedian, D.H., Fasano, A., Ashwood, P., and Mazmanian, S.K. (2021). Plasma and Fecal Metabolite Profiles in Autism Spectrum Disorder. Biol. Psychiatry *89*, 451-462. 10.1016/j.biopsych.2020.09.025.

28. Hsiao, E.Y., McBride, S.W., Hsien, S., Sharon, G., Hyde, E.R., McCue, T., Codelli, J.A., Chow, J., Reisman, S.E., Petrosino, J.F., et al. (2013). Microbiota modulate behavioral and physiological abnormalities associated with neurodevelopmental disorders. Cell *155*, 1451-1463. 10.1016/j.cell.2013.11.024.

29. Sharon, G., Cruz, N.J., Kang, D.W., Gandal, M.J., Wang, B., Kim, Y.M., Zink, E.M., Casey, C.P., Taylor, B.C., Lane, C.J., et al. (2019). Human Gut Microbiota from Autism Spectrum Disorder Promote Behavioral Symptoms in Mice. Cell *177*, 1600-1618.e1617. 10.1016/j.cell.2019.05.004.

30. Chen, C.M., Wu, C.C., Huang, C.L., Chang, M.Y., Cheng, S.H., Lin, C.T., and Tsai, Y.C. (2022). *Lactobacillus plantarum* PS128 Promotes Intestinal Motility, Mucin Production, and Serotonin Signaling in Mice. Probiotics Antimicrob. Proteins *14*, 535-545. 10.1007/s12602-021-09814-3.

31. Cheng, J., Tong, J., Li, C., Wang, Z., Li, H., Ren, M., Song, J., Song, D., Xie, Q., and Liu, M. (2025). Probiotic Characterization of *Lactiplantibacillus paraplantarum* SDN1.2 and Its Anti-Inflammatory Effect on Klebsiella pneumoniae-Infected Mammary Glands. Vet. Sci. *12*, 323. 10.3390/vetsci12040323.

32. Mihailović, M., Soković Bajić, S., Arambašić Jovanović, J., Brdarić, E., Dinić, S., Grdović, N., Uskoković, A., Rajić, J., Đorđević, M., Tolinački, M., et al. (2024). Beneficial Effects of Probiotic *Lactobacillus paraplantarum* BGCG11 on Pancreatic and Duodenum Function in Diabetic Rats. Int. J. Mol. Sci. *25*, 7697. 10.3390/ijms25147697.

33. Kong, X.J., Liu, J., Liu, K., Koh, M., Sherman, H., Liu, S., Tian, R., Sukijthamapan, P., Wang, J., Fong, M., et al. (2021). Probiotic and Oxytocin Combination Therapy in Patients with Autism Spectrum Disorder: A Randomized, Double-Blinded, Placebo-Controlled Pilot Trial. Nutrients *13*, 1552. 10.3390/nu13051552.

34. Houdou, M., Jacobs, N., Coene, J., Azfar, M., Vanhoutte, R., Van den Haute, C., Eggermont, J., Daniëls, V., Verhelst, S.H.L., and Vangheluwe, P. (2023). Novel Green Fluorescent Polyamines to Analyze ATP13A2 and ATP13A3 Activity in the Mammalian Polyamine Transport System. Biomolecules *13*, 337. 10.3390/biom13020337.

35. Balint, B., Damasio, J., Magrinelli, F., Guerreiro, R., Bras, J., and Bhatia, K.P. (2020). Psychiatric Manifestations of *ATP13A2* Mutations. Mov. Disord. Clin. Pract. *7*, 838-841. 10.1002/mdc3.13034.

36. Sørensen, D.M., Holemans, T., van Veen, S., Martin, S., Arslan, T., Haagendahl, I.W., Holen, H.W., Hamouda, N.N., Eggermont, J., Palmgren, M., and Vangheluwe, P. (2018). Parkinson disease related ATP13A2 evolved early in animal evolution. PLoS One *13*, e0193228. 10.1371/journal.pone.0193228.

37. Lesca, G., Rudolf, G., Labalme, A., Hirsch, E., Arzimanoglou, A., Genton, P., Motte, J., de Saint Martin, A., Valenti, M.P., Boulay, C., et al. (2012). Epileptic encephalopathies of the Landau-Kleffner and continuous spike and waves during slow-wave sleep types: genomic dissection makes the link with autism. Epilepsia *53*, 1526-1538. 10.1111/j.1528-1167.2012.03559.x.

38. Biamino, E., Di Gregorio, E., Belligni, E.F., Keller, R., Riberi, E., Gandione, M., Calcia, A., Mancini, C., Giorgio, E., Cavalieri, S., et al. (2016). A novel 3q29 deletion associated with autism, intellectual disability, psychiatric disorders, and obesity. Am. J. Med. Genet. B Neuropsychiatr. Genet. *171b*, 290-299. 10.1002/ajmg.b.32406.

39. Vallipuram, J., Grenville, J., and Crawford, D.A. (2010). The E646D-ATP13A4 mutation associated with autism reveals a defect in calcium regulation. Cell. Mol. Neurobiol. *30*, 233-246. 10.1007/s10571-009-9445-8.

40. van Veen, S., Irala, D., Sakers, K., Savage, J., Séjourné, G., Bindu, D.S., Ausloos, E., Dhondt, H., Schoonvliet, N., Van den Haute, C., et al. (2025). Astrocytic polyamine transport by ATP13A4 tunes excitatory synaptic transmission. Preprint at medRxiv, https://doi.org/10.1101/2025.04.04.25325117.

41. Koh, W., Kwak, H., Cheong, E., and Lee, C.J. (2023). GABA tone regulation and its cognitive functions in the brain. Nat. Rev. Neurosci. *24*, 523-539. 10.1038/s41583-023-00724-7.

42. De Sales-Millán, A., Reyes-Ferreira, P., Aguirre-Garrido, J.F., Corral-Guillé, I., Barrientos-Ríos, R., and Velázquez-Aragón, J.A. (2024). Comprehensive Analysis of Gut Microbiota Composition and Functional Metabolism in Children with Autism Spectrum Disorder and Neurotypical Children: Implications for Sex-Based Differences and Metabolic Dysregulation. Int. J. Mol. Sci. *25*, 6701. 10.3390/ijms25126701.

43. Sgritta, M., Dooling, S.W., Buffington, S.A., Momin, E.N., Francis, M.B., Britton, R.A., and Costa-Mattioli, M. (2019). Mechanisms Underlying Microbial-Mediated Changes in Social Behavior in Mouse Models of Autism Spectrum Disorder. Neuron *101*, 246-259.e246. 10.1016/j.neuron.2018.11.018.

44. Yu, Y., Zhang, B., Ji, P., Zuo, Z., Huang, Y., Wang, N., Liu, C., Liu, S.J., and Zhao, F. (2022). Changes to gut amino acid transporters and microbiome associated with increased E/I ratio in *Chd8*$^{+/-}$ mouse model of ASD-like behavior. Nat. Commun. *13*, 1151. 10.1038/s41467-022-28746-2.

45. Chen, C.M., Wu, C.C., Kim, Y., Hsu, W.Y., Tsai, Y.C., and Chiu, S.L. (2024). Enhancing social behavior in an autism spectrum disorder mouse model: investigating the underlying mechanisms of *Lactiplantibacillus plantarum* intervention. Gut Microbes *16*, 2359501. 10.1080/19490976.2024.2359501.

46. Schwieger, F., and Tebbe, C.C. (1998). A new approach to utilize PCR-single-strand-conformation polymorphism for 16s rRNA gene-based microbial community analysis. Appl. Environ. Microbiol. *64*, 4870-4876. 10.1128/AEM.64.12.4870-4876.1998.

47. Rognes, T., Flouri, T., Nichols, B., Quince, C., and Mahé, F. (2016). VSEARCH: a versatile open source tool for metagenomics. PeerJ *4*, 22, e2584. 10.7717/peerj.2584.

48. Chen, S.F. (2023). Ultrafast one-pass FASTQ data preprocessing, quality control, and deduplication using fastp. iMeta *2*, 5, e107. 10.1002/imt2.107.

49. Li, H., and Durbin, R. (2009). Fast and accurate short read alignment with Burrows-Wheeler transform. Bioinformatics *25*, 1754-1760. 10.1093/bioinformatics/btp324.

50. Li, D.H., Liu, C.M., Luo, R.B., Sadakane, K., and Lam, T.W. (2015). MEGAHIT: an ultra-fast single-node solution for large and complex metagenomics assembly via succinct de *Bruijn* graph. Bioinformatics *31*, 1674-1676. 10.1093/bioinformatics/btv033.

51. Hyatt, D., Chen, G.L., LoCascio, P.F., Land, M.L., Larimer, F.W., and Hauser, L.J. (2010). Prodigal: prokaryotic gene recognition and translation initiation site identification. BMC Bioinformatics *11*, 11, 119. 10.1186/1471-2105-11-119.

52. Li, W.Z., and Godzik, A. (2006). Cd-hit: a fast program for clustering and comparing large sets of protein or nucleotide sequences. Bioinformatics *22*, 1658-1659. 10.1093/bioinformatics/btl158.

53. Li, R.Q., Yu, C., Li, Y.R., Lam, T.W., Yiu, S.M., Kristiansen, K., and Wang, J. (2009). SOAP2: an improved ultrafast tool for short read alignment. Bioinformatics *25*, 1966-1967. 10.1093/bioinformatics/btp336.

54. Buchfink, B., Reuter, K., and Drost, H.G. (2021). Sensitive protein alignments at tree-of-life scale using DIAMOND. Nat. Methods *18*, 366-368. 10.1038/s41592-021-01101-x.

55. Hao, Y.H., Hao, S., Andersen-Nissen, E., Mauck, W.M., III, Zheng, S.W., Butler, A., Lee, M.J., Wilk, A.J., Darby, C., Zager, M., et al. (2021). Integrated analysis of multimodal single-cell data. Cell *184*, 3573-3587. 10.1016/j.cell.2021.04.048.

56. Zappia, L., and Oshlack, A. (2018). Clustering trees: a visualization for evaluating clusterings at multiple resolutions. GigaScience *7*, 9. 10.1093/gigascience/giy083.

57. Hu, C.X., Li, T.Y., Xu, Y.Q., Zhang, X.X., Li, F., Bai, J., Chen, J., Jiang, W.Q., Yang, K.Y., Ou, Q., et al. (2023). CellMarker 2.0: an updated database of manually curated cell markers in human/mouse and web tools based on scRNA-seq data. Nucleic Acids Res. *51*, D870-D876. 10.1093/nar/gkac947.

58. Wu, T.Z., Hu, E.Q., Xu, S.B., Chen, M.J., Guo, P.F., Dai, Z.H., Feng, T.Z., Zhou, L., Tang, W.L., Zhan, L., et al. (2021). clusterProfiler 4.0: A universal enrichment tool for interpreting omics data. The Innovation *2*, 3, 100141. 10.1016/j.xinn.2021.100141.

59. Hayamizu, T.F., Mangan, M., Corradi, J.P., Kadin, J.A., and Ringwald, M. (2005). The adult mouse anatomical dictionary: a tool for annotating and integrating data - art. no. R29. Genome Biol. *6*, 8, R29. 10.1186/gb-2005-6-3-r29.

60. Huang, W., Liao, C.-C., Han, Y., Lv, J., Lei, M., Li, Y., Lv, Q., Dong, D., Zhang, S., Pan, Y.-H., and Luo, J. (2020). Co-activation of Akt, Nrf2, and NF-κB signals under UPRER in torpid *Myotis ricketti* bats for survival. Communications Biology *3*, 658. 10.1038/s42003-020-01378-2.

61. Corcoran, B.M., Stanton, C., Fitzgerald, G.F., and Ross, R.P. (2005). Survival of probiotic lactobacilli in acidic environments is enhanced in the presence of metabolizable sugars. Appl. Environ. Microbiol. *71*, 3060-3067. 10.1128/aem.71.6.3060-3067.2005.

62. Azat, R., Liu, Y., Li, W., Kayir, A., Lin, D.B., Zhou, W.W., and Zheng, X.D. (2016). Probiotic properties of lactic acid bacteria isolated from traditionally fermented Xinjiang cheese. J. Zhejiang Univ.-SCI. B *17*, 597-609. 10.1631/jzus.B1500250.

63. Tiklová, K., Björklund, Å.K., Lahti, L., Fiorenzano, A., Nolbrant, S., Gillberg, L., Volakakis, N., Yokota, C., Hilscher, M.M., Hauling, T., et al. (2019). Single-cell RNA sequencing reveals midbrain dopamine

695 neuron diversity emerging during mouse brain development. Nat. Commun. *10*, 581. 10.1038/s41467-
696 019-08453-1.

697 64. Bhattacherjee, A., Djekidel, M.N., Chen, R., Chen, W., Tuesta, L.M., and Zhang, Y. (2019). Cell type-
698 specific transcriptional programs in mouse prefrontal cortex during adolescence and addiction. Nat.
699 Commun. *10*, 4169. 10.1038/s41467-019-12054-3.

700 65. Liu, H., Zhou, J., Tian, W., Luo, C., Bartlett, A., Aldridge, A., Lucero, J., Osteen, J.K., Nery, J.R., Chen,
701 H., et al. (2021). DNA methylation atlas of the mouse brain at single-cell resolution. Nature *598*, 120-
702 128. 10.1038/s41586-020-03182-8.

703 66. Hing, B., Mitchell, S.B., Filali, Y., Eberle, M., Hultman, I., Matkovich, M., Kasturirangan, M., Johnson, M.,
704 Wyche, W., Jimenez, A., et al. (2024). Transcriptomic Evaluation of a Stress Vulnerability Network Using
705 Single-Cell RNA Sequencing in Mouse Prefrontal Cortex. Biol. Psychiatry *96*, 886-899.
706 10.1016/j.biopsych.2024.05.023.

707

708 **STAR★METHODS**

709 **KEY RESOURCES TABLE**

| REAGENT OR RESOURCE | SOURCE | IDENTIFIER |
|---|---|---|
| Antibodies | | |
| ZO-1 Monoclonal Antibody | Thermo Fisher | Cat# ZO1-1A12; RRID: AB_2533147 |
| Goat anti-Mouse IgG (H+L) Cross-Adsorbed Secondary Antibody, Alexa Fluor™ 546 | Thermo Fisher | Cat# A-11003; RRID: AB_2534071 |
| ATP13A3 Antibody | Proteintech | Cat# 55108-1-AP; RRID: AB_3670238 |
| ATP13A2 Antibody | Santa Cruz | Cat# sc-293367 |
| β-Actin Antibody | Santa Cruz | Cat# sc-47778; RRID: AB_626632 |
| HRP-labeled Goat Anti-Mouse IgG (H+L) | Beyotime | Cat# A0216; RRID: AB_2860575 |
| HRP-labeled Goat Anti-Rabbit IgG (H+L) | Beyotime | Cat# A0208; RRID: AB_2892644 |
| Bacterial and virus strains | | |
| *Lactiplantibacillus plantarum* PS128 | Centro Sperimentale del Latte srl | Cat# G001723 |
| Chemicals, peptides, and recombinant proteins | | |
| Gelatins | Sinopharm | Cat# 10010326 |
| Sucrose | Sigma | Cat# V900116 |
| Fluorescein isothiocyanate (FITC)-dextran | Aladdin | Cat# F121152 |
| Ethanol | Aladdin | Cat# E118433-25L |
| Banana Extract | McCormick & Co., Inc. | N/A |
| Triton X-100 | Sigma | Cat# T8787-100ML |
| Goat Serum | Beyotime | Cat# C0265 |
| Bovine Serum Albumin | Sangon Biotech | Cat# A602440-0050 |
| Putrescine dihydrochloride | Sangon Biotech | Cat# A600793 |
| α-Difluoromethylornithine | MedChemExpress | Cat# HY-B0744 |
| Protease Inhibitor Cocktail | Roche | REF: 04693124001 |
| MRS broth | Solarbio | Cat# M8540 |
| Agar | Sangon Biotech | Cat# A505255-0250 |
| Lysozyme | Tiangen | Cat# RT401 |
| EDTA, disodium salt, dihydrate | Sangon Biotech | Cat# EB0185-500g |
| Carboxyfluorescein Diacetate Succinimidyl Ester | MedChemExpress | Cat# HY-D0938 |
| Simulated Gastric Fluid | Phygene | Cat# PH1840 |
| Simulated Intestinal Fluid | Phygene | Cat# PH1841 |
| Mineral Oil | Acmec | Cat# M97740 |
| Ethanol absolute | Sinopharm | Cat# 10009218 |
| Critical commercial assays | | |
| Hematoxylin and Eosin Staining Kit | Beyotime | Cat# C0105S |
| Alcian Blue Periodic Acid-Schiff Staining Kit | Leagene | Cat# DG0007 |
| Chemiluminescent HRP substrate | Millipore | Cat# WBKLS0500 |
| *TransZol* Up Plus RNA Kit | TransGen Biotech | Cat# ER501 |
| FastKing RT Kit (With gDNase) | Tiangen | Cat# KR116 |
| 2 x Taq Plus Master Mix II | Vazyme | Cat# P213-02 |
| SYBR Green Master Mix | Qiagen | Cat# 208054 |

| | | |
|---|---|---|
| Mouse Putrescine ELISA Kit | Enzyme-linked | REF: YJ523211 |
| Deposited data | | |
| Metagenomic sequencing | NCBI | BioProject: PRJNA1345245 |
| 16S rRNA Gene sequencing | NCBI | BioProject: PRJNA1345244 |
| Single-nucleus RNA sequencing | NCBI | BioProject: PRJNA1345209 |
| Whole-genome sequencing of *Lactiplantibacillus plantarum* PS128 | NCBI | BioProject: PRJNA1345344 |
| Targeted metabolomics assay | N/A | Tables S1 and S2 |
| Experimental models: Organisms/strains | | |
| Mouse: C57BL/6J | Shanghai Jihui Laboratory Animal Care Co., Ltd. | Cat# SHJH-M-01002 |
| Mouse: FVB.129P2-*Pde6b*$^{+}$ *Tyr*$^{c\text{-}ch}$ *Fmr1*$^{tm1Cgr/}$J | The Jackson Laboratory | RRID: IMSR_JAX:004624 |
| Oligonucleotides | | |
| Primers for *Lactiplantibacillus plantarum* PS128 quantitative real-time PCR, see Figure S3V | This paper | N/A |
| Primers for all bacteria quantitative real-time PCR, see Figure S3V | Schwieger and Tebbe[46] | https://doi.org/10.1128/AEM.64.12.4870-4876.1998 |
| Software and algorithms | | |
| Any-maze system (version 7.20) | Stoelting | https://stoeltingco.com/Neuroscience/ANY-maze |
| GraphPad Prism (version 10.6.1) | GraphPad | www.graphpad.com |
| Adobe illustrator (version 30.1) | Adobe | www.adobe.com |
| ImageJ (version 1.54f) | National Institutes of Health | https://imagej.nih.gov/ij/ |
| R (version 4.4.3) | R Core Team | https://www.r-project.org/ |
| Rsudio | R studio | https://rstudio.com |
| ImageQuant TL software (version 7.0) | Amersham Biosciences | https://imagequanttl.software.informer.com/ |
| Bio-Rad CFX Maestro software (version 3.1.1517.0823) | Bio-Rad | https://www.bio-rad-china.com/ |
| LivingImage software (version 4.5.2) | PerkinElmer | https://www.perkinelmer.com/lab-products-and-services/resources/in-vivo-imaging-software-downloads.html#LivingImage |
| Vsearch software (version 2.15.2) | Rognes et al[47] | https://github.com/torognes/vsearch/ |
| Silva database (version 123) | Leibniz Institute | ftp://download.nmdc.cn/tools/amplicon/silva/silva_16s_v123.fa.gz |
| OmicStudio cloud platform | OmicStudio | https://www.omicstudio.cn |
| Majorbio Cloud Platform | Majorbio | www.majorbio.com |
| FASTP (version 0.23.0) | Chen[48] | https://github.com/OpenGene/fastp/ |
| BWA (version 0.7.17) | Li and Durbin[49] | https://bio-bwa.sourceforge.net/ |
| MEGAHIT (version 1.1.2) | Li et al[50] | https://github.com/voutcn/megahit/ |
| Prodigal (version2.6.3) | Hyatt[51] | https://github.com/hyattpd/Prodigal/ |
| CD-HIT (version 4.7) | Li and Godzik[52] | http://weizhongli-lab.org/cd-hit |

| | | |
|---|---|---|
| SOAPaligner (version 2.21) | Li et al[53] | https://github.com/ShujiaHuang/SOAPaligner/ |
| NCBI NR database | NCBI | https://ftp.ncbi.nlm.nih.gov/blast/db/FASTA/ |
| DIAMOND (version 2.0.13) | Buchfink[54] | http://ab.inf.uni-tuebingen.de/software/diamond/ |
| KEGG Database | Kanehisa Laboratories | https://www.kegg.jp/kegg |
| CapCut (version 5.7.0) | Shenzhen Myotee Science and Technology Co., Ltd. | https://www.capcut.cn/ |
| Seurat (version 4.4.3) | Hao et al[55] | https://github.com/satijalab/seurat |
| Clustree (version 0.5.1) | Zappia and Oshlack[56] | https://github.com/lazappi/clustree |
| CellMarker 2.0 database | Hu et al[57] | http://117.50.127.228/CellMarker/CellMarker_download.html |
| scCustomize (version 3.2.0) | Marsh | https://github.com/samuel-marsh/scCustomize |
| ggplot2 (version 3.5.2) | Wickham et al | https://cran.r-project.org/package=ggplot2 |
| VennDiagram (version 1.7.3) | Chen | https://CRAN.R-project.org/package=VennDiagram |
| clusterProfiler (version 4.14.6) | Wu et al[58] | https://github.com/YuLab-SMU/clusterProfiler |
| org.Mm.eg.db (version 3.20.0) | Carlson | https://bioconductor.org/packages/release/data/annotation/html/org.Mm.eg.db.html |
| JAX Gene Ontology Database | Hayamizu et al[59] | https://www.informatics.jax.org/vocab/gene_ontology/GO:0008150 |

## EXPERIMENTAL MODEL AND STUDY PARTICIPANT DETAILS

### Animals and Ethical Statement

All animal procedures were approved by the Institutional Animal Care and Use Committee of East China Normal University (approval no. m20241106) and were conducted in accordance with institutional guidelines. Female C57BL/6J mice were obtained from Shanghai Jihui Laboratory Animal Care Co., Ltd., and male *Fmr1* knockout (KO) mice (stock no. 004624) were obtained from The Jackson Laboratory. To generate *Fmr1* KO mice on a uniform C57BL/6J genetic background, the KO line was backcrossed with wild-type C57BL/6J mice for ten generations. Male wild-type and *Fmr1* KO littermates on a C57BL/6J background were used for all experiments. Mice were housed in groups of six under specific pathogen-free (SPF) conditions at the multifunctional platform for innovation (Platform 101). The animal facility was maintained at 22 ± 1°C and 50 ± 5% relative humidity under a twelve-hour light/twelve-hour dark cycle (lights on at 6:00 a.m. and off at 6:00 p.m.). All mice had ad libitum access to water and a standard chow diet, with daily food intake set at 2.5 g per mouse from 1 month of age and 3.0 g per mouse from 2 months of age onward.

### Bacterial Strains and Growth Conditions

*Lactiplantibacillus plantarum* PS128 was obtained from Centro Sperimentale del Latte Srl and cultured in de Man-Rogosa-Sharpe (MRS) broth at 37 °C for liquid cultures or on MRS agar plates supplemented with 1.5% (w/v) agar.

730 ## METHOD DETAILS

731 ### Preparation of Jelly Enriched with PS128, Blank Controls, and FITC

732 Gelatin-based jellies were prepared as follows. Briefly, 2.1 g of gelatin and 0.3 g of sucrose were dissolved
733 in 22.5 mL of sterilized double-distilled water ($ddH_2O$) by heating to 55°C under constant stirring. The
734 solution was then diluted with sterilized $ddH_2O$ prewarmed to 55°C to a final volume of 30 mL while
735 continuously stirred.

736 The gelatin solution was evenly divided into two sterilized glass beakers and one 50-mL centrifuge tube
737 (10 mL each) and maintained at 37°C. Lyophilized *Lactiplantibacillus plantarum* PS128 (0.46 g) was added
738 to one beaker, and fluorescein isothiocyanate (FITC)–dextran (0.6 g) was added to the centrifuge tube. All
739 procedures involving FITC were performed under light-protected conditions. Both beakers were placed on
740 magnetic stirrers in a laminar-flow hood, whereas the centrifuge tube was mixed using a Genie 2 vortex
741 mixer until fully homogenized. Aliquots of 150 μL from the PS128-enriched and blank gelatin solutions and
742 300 μL from the FITC–dextran solution were dispensed into sterilized custom-made 0.5-mL jelly molds. The
743 molds (0.9 cm in diameter and 1.2 cm in height) were generated by trimming the upper portion of 2-mL
744 cryogenic vials with conical round bottoms. The filled molds were incubated at 4°C for 2 hours to allow
745 complete gelation.

746 After solidification, jellies were removed from the molds using sterilized tweezers. Each mouse was
747 provided with one PS128-enriched jelly containing approximately $2.07 \times 10^9$ colony-forming units (CFU) of
748 *Lactiplantibacillus plantarum* PS128 once every two days. FITC-enriched jellies were prepared fresh as
749 needed, and each mouse was provided with one jelly delivering 0.018 g of FITC–dextran per 30-g body
750 weight.

751

752 ### Training Mice for Voluntary Jelly Intake

753 Male wild-type (WT) and *Fmr1* knockout (KO) littermates at 3 weeks of age were housed separately for 1
754 week and then randomly assigned to four groups: WT, WTPS, KO, and KOPS. Mice in the WTPS and
755 KOPS groups were provided with one PS128-enriched jelly every two days, whereas mice in the WT and
756 KO groups were provided with one blank jelly on the same schedule (Video S1). To facilitate recognition
757 and voluntary consumption of the jelly, the jelly surface was lightly coated with powdered standard chow
758 during the first three feeding sessions.

759

760 ### Behavioral Experiments

761 Behavioral testing was initiated after 28 consecutive days of exposure to PS128-enriched jelly or blank jelly.
762 All tests were conducted between 9:00 a.m. and 3:00 p.m., with a minimum 2-day interval between
763 consecutive tests to minimize stress. Prior to behavioral assessment, mice were handled for 10 minutes
764 per day for 3 consecutive days and acclimated to the testing room for 2 hours on the test day.

765 Behavioral assays were performed in the following order: open-field test, novel object recognition test,
766 elevated plus maze test, O-maze test, reciprocal social interaction test, olfactory habituation/dishabituation
767 test, tube test, and balance beam test. Mouse behavior during training and testing sessions was recorded
768 using the ANY-maze behavioral tracking system (version 7.20) and/or video cameras. All apparatuses were
769 cleaned with 35% ethanol between individual mice, and a 5-minute interval was allowed between sessions
770 to dissipate residual odors.

771 #### *The open-field test*

772 The open-field test was performed in a square arena with white opaque walls (40 cm × 40 cm × 40 cm).
773 Mice were gently placed in the center of the arena and allowed to explore individually for 5 minutes under
774 an illumination of 45 lux. Total distance traveled and time spent in the center zone (20 cm × 20 cm) were
775 quantified.

776 #### *Novel object recognition test*

777 The test was performed in the same arena used for the open-field test under an illumination of 3 to 5 lux.
778 The test consisted of two 10-minute sessions separated by a 1-hour interval. During the first session

(learning phase), mice were allowed to freely explore the arena containing two identical objects (Object A1 and Object A2; 6 × 6 × 10 cm, length × width × height). After the 1-hour interval, mice were reintroduced to the arena for the second session (testing phase), during which one familiar object was replaced with a novel object of identical dimensions (Object B). Sniffing behavior was defined as the mouse directing its nose toward an object at a distance within 3 cm. The total duration and frequency of sniffing the novel object were quantified and compared with those for the familiar object. Climbing behavior was quantified as the total duration and frequency of climbing onto Objects A and B and was defined as any event in which both hind limbs were off the ground. The recognition index was calculated as the percentage of time spent sniffing the novel object relative to the total sniffing time.

***Elevated plus maze test***

The elevated plus maze consisted of a plus-shaped platform with two enclosed arms (30 cm × 5 cm) surrounded by 15 cm-high walls and two open arms (30 cm × 5 cm). The maze was elevated 60 cm above the floor. At the start of the test, mice were placed in the central area of the maze facing an open arm and allowed to explore freely for 5 minutes under an illumination of 45 lux. The time spent and distance traveled in the open and enclosed arms were quantified.

***The O-maze test***

The O-maze test was performed using a circular elevated track constructed of gray acrylic, with a height of 40 cm, an inner diameter of 48 cm, and a width of 5 cm. The maze consisted of two open arms and two enclosed arms of equal length arranged alternately along the track, with each arm spanning 45°. The open arms were equipped with 0.5 cm-high acrylic strips serving as anti-fall guardrails, whereas the enclosed arms were surrounded by 15 cm-high walls to block visual access to the external environment.

At the start of the test, each mouse was placed facing an enclosed arm and allowed to explore freely for 5 minutes under an illumination of 45 lux. Time spent, distance traveled, and the number of entries into the open and enclosed arms were quantified.

***Balance beam test***

The test was performed using an inclined square wooden beam with a flat surface. For the 30° condition, the beam was 0.8 cm wide and 100 cm long, with the lower and higher ends positioned at vertical heights of 26 cm and 76 cm, respectively. A black shelter box (12 × 12 × 12 cm; wall thickness, 3 mm) containing nesting material previously used by the mice for 3 days was placed at the higher end of the beam.

During the training phase, mice were placed at the lower end of the 30° beam and guided to traverse the beam once per day for 3 consecutive days. If a mouse paused for more than 10 seconds without forward movement, it was gently encouraged to proceed using the back of the experimenter's index finger. During the testing phase, mice traversed the beam without guidance and were allowed to rest in the shelter box for 15 seconds after crossing. Each mouse completed four trials on the 30° beam. The beam was then replaced with a narrower beam (0.6 cm wide and 50 cm long), with the lower and higher ends positioned at 33 cm and 76 cm, respectively, resulting in a 60° incline. Mice completed one trial on the 60° beam, and the latency to traverse the beam was recorded.

Performance was scored on a 7-point scale. A full score of 7 was assigned when a mouse crossed the beam without slipping, falling, or requiring prompting. One point was deducted for each occurrence of slipping, falling, or prompting, with a minimum score of 1.

***Reciprocal social interaction test***

The test was performed in the same arena used for the open-field test. The test consisted of three 3-minute sessions separated by 30-minute rest intervals. In each session, the experimental mouse was placed in the arena and allowed to interact with an age-, sex-, and weight-matched conspecific.

During the first session, the experimental mouse interacted with an unfamiliar wild-type (WT) mouse (Mouse 1). After a 30-minute rest interval, the experimental mouse was reintroduced to the arena to interact with the same WT mouse (Mouse 1), which had become familiar, during the second session. Following a second 30-minute rest interval, the experimental mouse interacted with a different unfamiliar WT mouse

827 (Mouse 2) during the third session. Social behaviors, including chasing, physical contact, sniffing within a
828 2-cm interaction zone, and crawling over WT mouse were quantified.
829 ***Olfactory habituation/dishabituation test***
830 The olfactory habituation/dishabituation test was performed in a clean, transparent cage (27.2 × 17.5 ×
831 11.5 cm, length × width × height) lined with fresh bedding and covered with a lid containing a 5-mm-diameter
832 hole for odor presentation. Each mouse was placed in the cage and allowed to acclimate for 90 seconds
833 before testing.
834 During testing, a cotton swab saturated with 100 μL of a given odor was introduced through the hole and
835 suspended in the cage for 1 minute. The swab was replaced every minute with a fresh one, resulting in
836 three consecutive presentations per odor. This procedure was repeated sequentially for four odors: pure
837 water, imitation banana flavor (1:100 dilution), and soiled bedding collected from two independent cages,
838 each housing two sibling wild-type (WT) mice.
839 Water and banana flavor were used as nonsocial odors. Soiled bedding from sex- and age-matched WT
840 mice was used as a social odor. Social odor samples were obtained from two distinct cages of sibling WT
841 mice that had been co-housed for at least 7 days, ensuring different family lineages between cages. Odors
842 were collected by rubbing a cotton swab along the bottom surface of each cage in a circular motion six
843 times.
844 The duration of sniffing, nibbling, reaching toward, and maintaining contact with the swab was quantified,
845 and the proportion of each behavior relative to the total interaction time was calculated (Videos S2 and S3).
846 ***Tube test***
847 The tube test was performed using a transparent acrylic tube (30 cm in length, 3 cm inner diameter, 3 mm
848 wall thickness). To facilitate habituation, two identical 15 cm tubes were placed in the home cages for three
849 consecutive days. Mice were then trained to traverse the 30 cm tube six times per day (three passes in
850 each direction) for three consecutive days.
851 On the testing day, weight-matched mice from different experimental groups (WT vs. KO, WT vs. WTPS,
852 WT vs. KOPS, or KO vs. KOPS) were placed at opposite ends of a horizontally positioned tube and allowed
853 to enter simultaneously. The mouse that advanced through the tube was assigned a score of 1, whereas
854 the mouse that retreated was assigned a score of 0. After an interval of 2 hours, a second trial was
855 conducted, pairing mice with similar first-trial scores and body weights.
856
857 **Intestinal Permeability Assay**
858 Four-month-old mice were fasted for 4 hours before actively consuming FITC–dextran–enriched jelly at a
859 dose of 0.6 mg per g body weight. Four hours after jelly consumption, approximately 800 μL of venous
860 blood was collected from each mouse via orbital blood sampling under isoflurane anesthesia and
861 transferred to a 1.5-mL microcentrifuge tube. Blood samples were allowed to clot at 25°C for 1 hour,
862 followed by centrifugation at 3,000 rpm for 10 minutes. The supernatant was carefully transferred to a clean
863 1.5-mL microcentrifuge tube and centrifuged again at 12,000 rpm for 10 minutes at 4°C.
864 A total of 200 μL of clarified serum was mixed with an equal volume of phosphate-buffered saline (PBS),
865 and 150 μL of the diluted serum was added in duplicate to a 96-well flat-bottom black microplate.
866 Fluorescence intensity of FITC–dextran in serum was measured using a spectrofluorometer at excitation
867 and emission wavelengths of 485 nm and 528 nm, respectively. A standard curve was generated using
868 serial dilutions of FITC–dextran in PBS (0, 1.0, 2.0, 4.0, and 6.0 × $10^{-4}$ μg/μL), and serum FITC–dextran
869 concentrations were calculated by interpolation according to the manufacturer's instructions.
870
871 **Histological Evaluation of Transverse Colon**
872 Colon segments (1.5 cm in length, located 1.5–3.0 cm proximal to the distal colon) were excised and fixed
873 in 4% paraformaldehyde in phosphate-buffered saline (PBS; pH 7.4) at 4°C for 24 hours. After fixation,
874 tissues were washed in PBS, dehydrated through a graded ethanol series, and embedded in paraffin.

875 Paraffin-embedded samples were sectioned at a thickness of 5 μm and mounted onto adhesive microscope
876 slides.
877 Sections were deparaffinized, rehydrated, and stained with hematoxylin and eosin (H&E) or Alcian blue–
878 periodic acid–Schiff (AB–PAS). Images were acquired using an LED-illuminated light microscope. For
879 quantitative analysis, three consecutive intact crypts per section, defined as fully visible and undamaged
880 structures, were randomly selected. Measurements were performed on at least three independent sections
881 per mouse.
882
883 **Immunofluorescence Assay**
884 Paraffin-embedded sections were subjected to antigen retrieval by incubation in sodium citrate buffer (10
885 mM, pH 6.0) at 99°C for 15 minutes. Sections were then blocked in a solution containing 0.5% Triton X-
886 100, 5% goat serum, and 5% bovine serum albumin for 2 hours at room temperature. After blocking,
887 sections were incubated with a primary antibody against ZO-1 (1:200) at 4°C for 36 hours. Following rinsing
888 in phosphate-buffered saline (PBS), sections were incubated with an appropriate secondary antibody
889 (1:500) for 2 hours at 37°C. Fluorescent signals were imaged using a confocal laser scanning microscope
890 with excitation and emission wavelengths of 557 nm and 572 nm, respectively.
891
892 **Treatment Protocols for DFMO and Putrescine**
893 α-Difluoromethylornithine (DFMO) and putrescine dihydrochloride were dissolved in sterile saline at room
894 temperature and administered via intraperitoneal injection (i.p.). For juvenile *Fmr1* knockout (KO) mice,
895 DFMO treatment was initiated at 4 weeks of age at a dose of 500 mg per kg body weight, administered
896 every other day for 28 days. After mice reached 2 months of age, DFMO administration was continued
897 throughout the behavioral testing period until tissue collection. For adult mice, *Fmr1* KO mice received
898 DFMO at a dose of 500 mg per kg body weight once daily for 7 consecutive days, whereas adult wild-type
899 (WT) mice received putrescine dihydrochloride at a dose of 200 mg per kg body weight once daily for 7
900 consecutive days. Treatments were maintained throughout behavioral testing until tissue collection.
901
902 **Determination of Putrescine in Prefrontal Cortex**
903 Following behavioral assessments, mice were euthanized under deep isoflurane anesthesia, and the
904 prefrontal cortex (PFC) was rapidly dissected and weighed. Tissue homogenates were prepared by adding
905 lysis buffer at a ratio of 500 μL per 0.1 g of tissue, followed by homogenization and incubation on ice for 10
906 minutes. Homogenates were centrifuged at 12,000 rpm for 5 minutes at 4°C, and the supernatant was
907 collected for putrescine quantification.
908 Putrescine concentrations were measured using a commercial enzyme-linked immunosorbent assay
909 (ELISA) kit according to the manufacturer's instructions. Samples were diluted 1:5 in dilution buffer, and 50
910 μL of each diluted sample or standard was added to pre-coated wells together with 100 μL of horseradish
911 peroxidase (HRP)–conjugated detection antibody. After incubation for 60 minutes at 37°C, wells were
912 washed five times, followed by the addition of substrate solution and incubation in the dark for 15 minutes.
913 The reaction was terminated with stop solution, and absorbance was measured at 450 nm. Putrescine
914 concentrations were calculated from a standard curve and corrected for the dilution factor.
915
916 **Immunoblotting**
917 Prefrontal cortex tissues were homogenized individually in ice-cold lysis buffer supplemented with a
918 protease inhibitor cocktail.[60] Protein concentrations were determined, and 20 μg of total protein per sample
919 was loaded onto 10% SDS–polyacrylamide gels for electrophoretic separation, followed by transfer onto
920 0.2-μm polyvinylidene difluoride (PVDF) membranes using an electroblotting system.

921 The PVDF membranes were blocked in TBST blocking buffer for 16 hours at 4°C, followed by incubation
922 overnight at 4°C with primary antibodies: anti-ATP13A3 (1:500), anti-ATP13A2 (1:200), and anti-β-actin
923 (1:10000).
924 Following three washes with TBST, the blots were incubated with goat anti-mouse IgG labeled with
925 horseradish peroxidase (HRP) (1:1000) or goat anti-rabbit IgG labeled with HRP (1:1000) and visualized
926 using a chemiluminescent HRP detection kit. Images of the blots were captured using the ImageQuant
927 LAS-4000 system, and the density of protein bands was quantified using ImageQuant TL software (version
928 7.0). The relative protein quantity was determined by normalizing the density of the target protein band to
929 the density of the β-actin band in the same lane. Western blot analysis included two or six technical
930 replicates for each sample.
931
932 **Fluorescent Labeling of PS128**
933 Overnight cultures of *Lactiplantibacillus plantarum* PS128 were inoculated into sterile MRS broth at a 1%
934 (v/v) ratio and grown to an optical density at 600 nm ($OD_{600}$) of 1.0. Bacterial cells were harvested by
935 centrifugation at 5,000 × g for 2 minutes at 4°C and washed three times with phosphate-buffered saline
936 (PBS). Carboxyfluorescein diacetate succinimidyl ester (CFDA/SE) was then added to a final concentration
937 of 20 μM, and bacteria were incubated in the dark at 37°C for 30 minutes. Excess dye was removed by
938 washing the cells three times with PBS.
939 Following labeling, PS128 cells were resuspended in PBS at concentrations of $1 \times 10^9$ or $1 \times 10^{10}$ colony-
940 forming units (CFU) per milliliter. A small aliquot of the bacterial suspension was mounted onto microscope
941 slides, and fluorescence images were acquired using a fluorescence microscope. Labeling efficiency was
942 calculated as the proportion of fluorescently labeled cells relative to the total number of cells. Quantification
943 was performed by randomly selecting seven fields of view from samples at $1 \times 10^9$ CFU/mL and three fields
944 of view from samples at $1 \times 10^{10}$ CFU/mL.
945
946 **Determination of PS128 Growth Before and After CFDA/SE Treatment**
947 PS128 cultures at a concentration of $1 \times 10^{10}$ colony-forming units (CFU) per milliliter, with or without
948 CFDA/SE labeling, were inoculated into sterile MRS broth at a 3% (v/v) ratio. Bacterial growth was
949 monitored by measuring the optical density at 600 nm ($OD_{600}$) every 30 minutes during the first 2 hours and
950 then every 1 hour up to 8 hours to generate growth curves. For each condition, $OD_{600}$ values at each time
951 point were calculated as the mean of two technical replicates from five independent bacterial cultures.
952
953 **Determination of PS128 Tolerance to Gastric and Intestinal Fluids**
954 Tolerance of *Lactiplantibacillus plantarum* PS128 to simulated gastric fluid (SGF) and simulated intestinal
955 fluid (SIF) was assessed based on previously described methods by Corcoran et al.[61] and Azat et al.[62], with
956 modifications. Briefly, PS128 cells resuspended in phosphate-buffered saline (PBS) were collected by
957 centrifugation at 5,000 × g for 2 minutes at 4°C and resuspended in 2.5 mL of MRS broth for a recovery
958 period of 2.5 hours.
959 An 800-μL aliquot of PS128 culture at a concentration of $1 \times 10^{10}$ colony-forming units (CFU) per milliliter
960 was mixed with an equal volume of MRS broth (control), a 1:1 mixture of MRS broth and SGF, or a 1:1
961 mixture of MRS broth and SIF. Cultures containing SGF were overlaid with mineral oil to maintain anaerobic
962 conditions and incubated statically for 3 hours, whereas cultures containing SIF were incubated with
963 shaking at 160 rpm for 4 hours. Cultures in MRS broth alone served as controls.
964 After incubation, 200 μL of each bacterial suspension at a $10^{-5}$ dilution was plated onto MRS agar plates.
965 Following incubation at 37°C for 24 hours, colonies were imaged and counted using ImageJ software
966 (version 1.54f). Tolerance was calculated as the percentage of colony-forming units recovered after SGF
967 or SIF exposure relative to the MRS control. Six independent experiments were performed for statistical
968 analysis.
969

970 **Detection and relative quantification of PS128 in fecal samples**
971 Fresh fecal samples were collected from 3.5-month-old mice and incubated with lysozyme (3 mg/mL) in
972 lysis buffer containing 10 mM Tris and 1 mM EDTA (pH 8.0) at 30ºC for 5 minutes to facilitate bacterial cell
973 lysis. Total RNA was isolated using TRIzol reagent according to the manufacturer's instructions.
974 Complementary DNA (cDNA) was synthesized using the FastKing RT kit following the manufacturer's
975 protocol. A positive control was prepared using 3 mL of PS128 culture at an optical density at $OD_{600}$ of 0.6.
976 PS128-specific primers (Figure S3V) for PCR and real-time reverse transcription quantitative PCR (RT-
977 *q*PCR) were designed based on the complete PS128 genome generated in this study and deposited in the
978 NCBI database (BioProject accession number PRJNA1345344). PCR amplification was performed using
979 2× Taq Plus Master Mix II with an initial denaturation step at 94ºC for 3 minutes, followed by 40 cycles of
980 denaturation at 94ºC for 30 seconds, annealing at 48ºC for 35 seconds, and extension at 72ºC for 25
981 seconds, with a final extension at 72ºC for 10 minutes. Ten microliters of each PCR product were resolved
982 on a 2% agarose gel and visualized under ultraviolet illumination using a gel documentation system.
983 RT-*q*PCR was performed using SYBR Green Master Mix on a CFX Connect Real-Time PCR Detection
984 System with 35 cycles consisting of denaturation at 95ºC for 5 seconds followed by annealing and extension
985 at 60ºC for 30 seconds. Data were analyzed using Bio-Rad CFX Maestro software (version 3.1.1517.0823).
986 Relative PS128 abundance was calculated using the $2^{-\Delta\Delta Ct}$ method, with bacterial 16S rRNA serving as the
987 internal reference.
988
989 **Imaging the Localization of PS128 in the Mouse Gut**
990 Adult mice in the PS128 group were administered 500 μL of fluorescently labeled PS128 ($1 \times 10^{10}$ CFU/mL)
991 by oral gavage once daily for 3 consecutive days, whereas control mice received 500 μL of phosphate-
992 buffered saline (PBS). After the final gavage, mice were divided into two groups for analysis.
993 For the first group, mice were anesthetized with isoflurane, and the abdominal area was shaved to
994 facilitate in vivo fluorescence imaging using an IVIS Lumina III Smart Imaging System. Following whole-
995 body imaging, mice were euthanized by cervical dislocation under deep isoflurane anesthesia, and the
996 entire gastrointestinal tract was immediately isolated. Ex vivo fluorescence imaging of the gut was
997 performed using the IVIS system with an excitation wavelength of 480 nm and an emission wavelength of
998 520 nm. Total and mean fluorescence intensities within defined regions of interest were quantified using
999 Living Image software (version 4.5.2).
1000 For the second group, mice were euthanized immediately after the final gavage. Segments of the
1001 gastrointestinal tract were collected, including a 10-cm segment of the small intestine proximal to the
1002 stomach, the cecum, and a 1.5-cm segment of the distal colon near the anus. Tissues were cut into
1003 approximately 5-mm squares and imaged using a stereoscopic fluorescence microscope. Mean
1004 fluorescence intensity was quantified using ImageJ software.
1005
1006 **Whole-genome sequencing and annotation of *Lactiplantibacillus plantarum* PS128**
1007 Whole-genome sequencing of *Lactiplantibacillus plantarum* PS128 was performed by BGI Genomics Co.,
1008 Ltd. (Shenzhen, China) using a hybrid sequencing strategy. Long-read sequencing was conducted on the
1009 PacBio RS II platform, and short-read sequencing was performed on the Illumina HiSeq 4000 platform.
1010 PacBio subreads shorter than 1 kb were removed during quality filtering. Error correction was performed
1011 using Pbdagcon, and corrected reads were assembled into draft contigs using the Celera Assembler.
1012 Illumina short reads were subsequently used to polish the assembly and improve base accuracy.
1013 Gene prediction was performed using Glimmer3. Transfer RNAs, ribosomal RNAs, and small RNAs were
1014 identified using standard RNA annotation tools. Tandem repeats, genomic islands, prophage regions, and
1015 CRISPR arrays were identified using established bioinformatics pipelines.
1016 Functional annotation of predicted genes was conducted by sequence similarity searches against public
1017 databases, including KEGG, COG, NR, Swiss-Prot, GO, TrEMBL, and EggNOG. Genes associated with

virulence, antimicrobial resistance, host–pathogen interaction, and carbohydrate metabolism were annotated using specialized databases.

Comparative genomic analyses were performed against representative *Lactiplantibacillus* genomes using whole-genome alignment and clustering approaches. Core and pan-genome analyses were conducted using CD-HIT, and phylogenetic relationships were inferred based on whole-genome comparisons. Whole-genome sequencing data for PS128 have been deposited in the NCBI database (BioProject accession number PRJNA1345344).

## 16S rRNA Gene Sequencing and analysis

DNA extraction, PCR amplification, library construction, and sequencing were performed by Origin-gene Biotechnology Co., Ltd. (Shanghai, China). Fecal samples were collected from four mouse groups (WT, WTPS, KO, and KOPS) at 8:00 p.m. Microbial genomic DNA was extracted using the QIAamp Fast DNA Stool Mini Kit (Qiagen, Germany) and assessed by 1% agarose gel electrophoresis.

The V3–V4 region of the bacterial 16S rRNA gene was amplified by PCR using primers 338F (5'-ACTCCTACGGGAGGCAGCAG-3') and 806R (5'-GGACTACHVGGGTWTCTAAT-3'), each containing an eight-base sample-specific barcode. PCR was performed with an initial denaturation at 95°C for 3 minutes, followed by 27 cycles of denaturation at 95°C for 30 seconds, annealing at 55°C for 30 seconds, and extension at 72°C for 45 seconds, with a final extension at 72°C for 10 minutes. Reactions were carried out in triplicate 20-μL volumes containing 5× FastPfu Buffer, dNTPs, primers, FastPfu Polymerase, and 10 ng of template DNA. Amplicons were excised from 2% agarose gels and purified using the AxyPrep DNA Gel Extraction Kit (Axygen Biosciences, USA).

Sequencing libraries were prepared using the NEBNext Ultra DNA Library Prep Kit for Illumina (NEB, USA) according to the manufacturer's instructions. Library quality was assessed using a Qubit 2.0 Fluorometer (Thermo Scientific, USA) and an Agilent Bioanalyzer 2100 system. Paired-end sequencing (PE250) was performed on an Illumina NovaSeq 6000 platform. The 16S rRNA gene sequencing data have been deposited in the NCBI Sequence Read Archive (BioProject accession number PRJNA1345244).

Raw sequencing data were processed using VSEARCH (version 2.15.2) on a Linux platform. After removal of primers and low-quality reads, sequences were merged, dereplicated, and clustered into operational taxonomic units (OTUs) at 97% sequence similarity, with chimeric sequences removed based on the RDP Gold database. An OTU abundance table was generated, and taxonomic classification was assigned using the SILVA reference database (release 126).

Downstream analyses were performed in R. The OTU table and taxonomic annotations were imported into a phyloseq object. Alpha-diversity metrics, including observed species, Shannon index, and Simpson index, were calculated using the microbiome package. Beta-diversity analyses were conducted based on Bray–Curtis and UniFrac distances, followed by principal coordinates analysis using the vegan package. Differentially abundant taxa were identified using LEfSe analysis implemented on the OmicStudio platform (https://www.omicstudio.cn), and data visualization was performed using ggplot2.

## Metagenomic Sequencing and Analysis

### *Sample preparation and sequencing*

Total genomic DNA was extracted from 0.2 g of fecal sample using the MagAttract PowerSoil Pro DNA Kit (Qiagen, Germany) according to the manufacturer's instructions. DNA concentration and purity were measured using a Quantus Fluorometer (PicoGreen, Promega, USA) and a NanoDrop 2000 spectrophotometer (Thermo Fisher Scientific, USA), respectively, and DNA integrity was assessed by 1% agarose gel electrophoresis.

Extracted DNA was fragmented to an average size of approximately 350 bp using a Covaris M220 Focused-ultrasonicator for paired-end library construction. Sequencing libraries were prepared using the NEXTFLEX Rapid DNA-Seq Kit (Bioo Scientific, USA) following the manufacturer's protocol and sequenced

1066 on an Illumina NovaSeq 6000 platform (S4 flow cell). DNA extraction, library construction, and sequencing
1067 were performed by Majorbio Bio-Pharm Technology Co., Ltd. (Shanghai, China). Metagenomic sequencing
1068 data have been deposited in the NCBI Sequence Read Archive (BioProject accession number
1069 PRJNA1345245).

1070 ***Metagenomic assembly and annotation***

1071 Raw sequencing reads were quality-filtered using FASTP (version 0.23.0) to remove low-quality reads and
1072 reads containing ambiguous bases. Host-derived reads were removed by alignment to the mouse reference
1073 genome using BWA (version 0.7.17). High-quality reads were assembled de novo using MEGAHIT (version
1074 1.1.2), and contigs ≥300 bp were retained. Open reading frames were predicted using Prodigal (version
1075 2.6.3), and a non-redundant gene catalog was generated using CD-HIT (version 4.7).

1076 Gene abundance was estimated by mapping quality-filtered reads back to the gene catalog using
1077 SOAPaligner (version 2.21). Taxonomic annotation was performed by aligning non-redundant genes to the
1078 NCBI non-redundant (NR) database using DIAMOND (version 2.0.13). Functional annotation was
1079 conducted based on the Kyoto Encyclopedia of Genes and Genomes (KEGG, www.kegg.jp) database.
1080 Data visualization and statistical analyses were performed in R using ggplot2.

1081 ***Reconstruction of metagenome-assembled genome (MAG) and gut-brain module (GBM) analysis***

1082 After quality control, removal of host-derived reads, and de novo assembly, contigs were binned into
1083 metagenome-assembled genomes (MAGs) using MetaBAT2 (version 2.15) based on sequence
1084 composition and coverage depth, yielding 1,297 bins. MAG quality was assessed using CheckM (version
1085 1.2.2) to estimate genome completeness and contamination. High-quality MAGs were defined as those
1086 with ≥ 50% completeness and ≤ 10% contamination; bins not meeting these thresholds were classified as
1087 low quality. Using these criteria, 533 high-quality MAGs were retained.

1088 To remove redundancy, high-quality MAGs were dereplicated using dRep (version 3.4.2), resulting in
1089 200 unique, non-redundant MAGs. Taxonomic assignment was performed using DIAMOND (version 2.0.13)
1090 against the NCBI Taxonomy database to define species-level genome bins (SGBs). Protein-coding genes
1091 within MAGs were annotated using DIAMOND against the NCBI non-redundant (NR) protein database.
1092 Functional annotation and enrichment analyses were performed using KofamKOALA (version 1.3.0) with
1093 the Kyoto Encyclopedia of Genes and Genomes (KEGG) database.

1094 Gut–brain modules (GBMs) encoded by SGBs were reconstructed based on curated definitions
1095 described by Valles-Colomer et al., 2019[25] and categorized into eight functional subgroups according to
1096 their roles. Visualization and plotting were performed in R using ggplot2 and Chiplot.

1097

1098 **Single-nucleus RNA sequencing**

1099 ***Frozen Tissue Nuclear Dissociation***

1100 Single-nucleus RNA sequencing (snRNA-seq) was performed by Shanghai Majorbio Bio-Pharm
1101 Technology Co., Ltd. (Shanghai, China). Frozen prefrontal cortex (PFC) tissues were homogenized using
1102 a glass Dounce tissue grinder (Sigma, USA) with 25 strokes of pestle A and 25 strokes of pestle B in 2 mL
1103 of ice-cold Nuclei EZ lysis buffer. The homogenate was incubated on ice for 5 minutes, followed by addition
1104 of 3 mL of cold lysis buffer and an additional 5-minute incubation. Nuclei were centrifuged at 500 × g for 5
1105 minutes at 4°C, washed with 5 mL of ice-cold lysis buffer, and incubated on ice for an additional 5 minutes.
1106 The nuclear pellet was resuspended and washed in 5 mL of nuclei suspension buffer (NSB; PBS
1107 supplemented with 0.01% BSA and 0.1% RNase inhibitor, Clontech, USA). Nuclei were resuspended in 2
1108 mL of NSB, filtered through a 35-μm cell strainer (Corning-Falcon, USA), and counted. Nuclei were loaded
1109 onto the 10x Genomics Chromium Controller at a final concentration of 1,000 nuclei per μL.

1110 ***10x library preparation and sequencing***

1111 Gel beads containing unique molecular identifiers (UMIs) and cell barcodes were loaded to near
1112 saturation such that each nucleus was paired with one bead in a Gel Bead-in-Emulsion (GEM). After lysis,
1113 polyadenylated RNA molecules hybridized to bead-bound oligonucleotides. Beads were collected for
1114 reverse transcription, during which each cDNA molecule was tagged at its 3' end (corresponding to the 5'

end of the mRNA) with a UMI and cell barcode. Subsequent steps included second-strand synthesis, adaptor ligation, and universal amplification. Sequencing libraries were prepared from randomly fragmented cDNA to enrich 3' transcript ends linked to barcodes and UMIs.

All procedures followed the Chromium Single Cell 3' Library & Gel Bead Kit v3.1 manufacturer's protocol. Libraries were quantified using a High Sensitivity DNA Chip (Agilent) on a Bioanalyzer 2100 and a Qubit High Sensitivity DNA Assay (Thermo Fisher Scientific), and sequenced on an Illumina NovaSeq X Plus using paired-end 150-bp chemistry. The snRNA-seq data have been deposited in the NCBI Sequence Read Archive (BioProject accession number PRJNA1345209).

***snRNA-seq data processing***

Raw reads were processed using Cell Ranger (version 7.1.0) with default parameters. FASTQ files generated from Illumina sequencing were aligned to the mouse GRCm39 genome (Ensembl release 111 annotation) using the STAR algorithm. Gene–barcode matrices were generated by counting UMIs and filtering non-cell-associated barcodes. The resulting matrix was imported into Seurat (version 4.4.3) for quality control and downstream analysis. Low-abundance genes were filtered such that only features expressed in at least three cells were retained. Cells were filtered using the following criteria: 200 to 6,000 detected genes per cell and mitochondrial gene percentage < 25% (PercentageFeatureSet). Data were normalized using NormalizeData, and the top 2,000 highly variable genes were identified using FindVariableFeatures. Principal component analysis (PCA) was performed, and 12 significant principal components (PCs) were selected based on the ElbowPlot function. A shared nearest-neighbor (SNN) graph was constructed using FindNeighbors, and clusters were identified using FindClusters at a resolution of 0.3, optimized with Clustree (version 0.5.1). Clusters were visualized in Uniform Manifold Approximation and Projection (UMAP) space.

Differentially expressed genes (DEGs) were identified using the Wilcoxon rank-sum test (FindAllMarkers). Cell types were annotated using a semi-automated strategy based on the CellMarker 2.0 database and published references by Tiklová et al.[63], Bhattacherjee et al.[64], Liu et al.,[65] and Hing et al.[66] Expression of *Atp13a2*, *Atp13a3*, and *Atp13a4* was visualized using FeaturePlot_scCustom in scCustomize (version 3.2.0) and ggplot2 (version 3.5.2).

***Differential expression analysis and functional enrichment***

DEGs were identified using FindMarkers with the following thresholds: genes expressed in ≥ 10% of cells, adjusted $P \leq 0.05$, and $|\log_2 FC| > 0.12$. VennDiagram (version 1.7.3) was used to identify genes significantly upregulated or downregulated in KOPS vs. KO (adjusted $P \leq 0.05$ and $|\log_2 FC| > 0.12$) but not significantly different from WT (adjusted $P > 0.05$).

Gene Ontology (GO) enrichment analysis was performed using enrichGO in clusterProfiler (version 4.14.6) after gene ID conversion with org.Mm.eg.db (version 3.20.0). Enriched Biological Process (BP) terms were defined at $q \leq 0.05$ (Benjamini–Hochberg adjusted) using annotations from the JAX Gene Ontology Database and visualized using ggplot2 (version 3.5.2).

## Targeted Metabolomics of Fatty Acids and Neurotransmitters in Serum and Brain

***Targeted metabolomics for fatty acids in brain***

Mice were anesthetized with isoflurane, after which venous blood was collected by ophthalmectomy. Brain tissues were then harvested, immediately frozen in liquid nitrogen, and stored at −80°C until analysis. Blood samples were allowed to stand at room temperature for 1 hour before centrifugation at 3,000 rpm for 10 minutes. The supernatant was centrifuged again at 12,000 rpm for 10 minutes at 4°C, and the resulting serum was collected and stored at −80°C until use. All targeted metabolomics analyses were performed by Shanghai BioTree Biomedical Technology Co., Ltd.

Brain tissues were transferred to 2-mL Eppendorf tubes and extracted with 1 mL of $H_2O$, followed by vortex mixing for 10 seconds. Samples were homogenized in a ball mill at 40 Hz for 4 minutes and sonicated for 5 minutes in an ice-water bath. Homogenization and sonication were repeated three times. Samples were centrifuged at 5,000 rpm for 20 minutes at 4°C, and 0.8 mL of the supernatant was transferred to a

1164 new 2-mL Eppendorf tube. To each tube, 0.1 mL of 50% $H_2SO_4$ and 0.8 mL of extraction solution (25 mg/L
1165 internal standard in methyl tert-butyl ether) were added. Samples were vortexed for 10 seconds, oscillated
1166 for 10 minutes, sonicated for an additional 10 minutes in an ice-water bath, and centrifuged at 10,000 rpm
1167 for 15 minutes at 4ºC. The supernatant was kept at −20ºC for 30 minutes and then transferred to 2-mL
1168 glass vials for GC–MS analysis.
1169 Quantification of fatty acids was performed using a SHIMADZU GC2030-QP2020 NX gas
1170 chromatograph–mass spectrometer equipped with an HP-FFAP capillary column. A 1-μL aliquot of each
1171 extract was injected in split mode (5:1). Helium was used as the carrier gas at a flow rate of 1.2 mL/minute,
1172 with a front inlet purge flow of 3 mL/minute. The oven temperature program was as follows: 50ºC for 1
1173 minute; ramp to 150ºC at 50ºC/minute (1-minute hold); ramp to 170ºC at 10ºC/minute; ramp to 225ºC at
1174 20ºC/minute (1-minute hold); and ramp to 240ºC at 40ºC/minute (1-minute hold). The injection port, transfer
1175 line, quadrupole, and ion source temperatures were set to 240ºC, 240ºC, 150ºC, and 200ºC, respectively.
1176 Electron impact ionization was performed at −70 eV, and spectra were acquired in Scan/SIM mode over an
1177 m/z range of 33–150 following a 3.75-minute solvent delay.
1178 ***Targeted metabolomics for neurotransmitters in serum and brain***
1179 For serum samples collected from isoflurane-anesthetized mice, 20 μL of serum was transferred to a 1.5-
1180 mL Eppendorf tube and mixed with 80 μL of precooled (−20ºC) extraction solvent (acetonitrile containing
1181 0.1% formic acid). Samples were vortexed for 30 seconds, sonicated for 15 minutes in an ice-water bath,
1182 incubated at −40°C overnight, and centrifuged at 12,000 rpm for 15 minutes at 4ºC.
1183 For brain samples, tissues were weighed and transferred to 1.5-mL Eppendorf tubes. Eighty microliters
1184 of precooled extraction solvent (acetonitrile containing 0.1% formic acid) and 20 μL of $H_2O$ were added,
1185 followed by vortexing for 30 seconds, homogenization at 45 Hz for 4 minutes, and sonication for 5 minutes
1186 in an ice-water bath. Homogenization and sonication were repeated three times. Samples were incubated
1187 at −20ºC overnight and centrifuged at 12,000 rpm for 15 minutes at 4ºC. Eighty microliters of each
1188 supernatant were mixed with 40 μL of 100 mM sodium carbonate and 40 μL of 2% benzoyl chloride in
1189 acetonitrile. After incubation for 30 minutes, 10 μL of internal standard was added, and samples were
1190 centrifuged at 12,000 rpm for 15 minutes at 4ºC. Forty microliters of the supernatant were diluted with 20
1191 μL of $H_2O$ and transferred to autosampler vials for UHPLC–MS/MS analysis.
1192 UHPLC separation was performed on an ACQUITY Premier System (Waters) equipped with an
1193 ACQUITY UPLC HSS T3 column (100 × 2.1 mm, 1.8 μm). The mobile phases were A: 0.1% formic acid
1194 and 1 mM ammonium acetate in water, and B: acetonitrile. The column temperature was maintained at
1195 40ºC, the autosampler temperature at 10ºC, and the injection volume was 1 μL. Mass spectrometric
1196 detection was conducted on a SCIEX Triple Quad™ 6500+ mass spectrometer with the following
1197 parameters: IonSpray Voltage, +5,000 V; Curtain Gas, 35 psi; Source Temperature, 400ºC; Ion Source Gas
1198 1 and 2, 60 psi. Data acquisition and processing were performed using SCIEX Analyst Workstation (version
1199 1.6.3) and Data Driven Flow (version 2.0.3.11).
1200
1201 **QUANTIFICATION AND STATISTICAL ANALYSIS**
1202 All behavioral and histological analyses were performed under blinded conditions. Statistical analyses were
1203 carried out using GraphPad Prism (GraphPad Software, version 10.6.1). Normality was assessed using the
1204 Shapiro–Wilk, D'Agostino–Pearson, Anderson–Darling, and Kolmogorov–Smirnov tests. Data are
1205 presented as mean ± SEM unless otherwise stated. Normally distributed data were compared using two-
1206 tailed (or one-tailed, as specified in figure legends) unpaired Student's *t*-tests. Non-normally distributed data
1207 were analyzed using two-tailed (or one-tailed, as specified) Mann–Whitney U tests. $P$ values < 0.05 were
1208 considered statistically significant. Exact sample sizes (n) and statistical tests used are reported in the figure
1209 legends, and precise $P$ values are indicated in the figures. All raw data used in this study are provided in
1210 Supplementary Tables S1 and S2.